Coversheet

This work is a *non-peer reviewed manuscript*.

It has been submitted to Volcanica journal (https://www.jvolcanica.org/), a Diamond Open Access Journal, and is currently under peer review.

The manuscript here is the revised one after reviewer's comments have been taken into account, and as of writing 05/07/2019 is being reconsidered by the journal.

We would happily receive any comments that might improve and add to the final version.

Title: The Leaning Puy de Dôme (Auvergne, France) tilted by shallow intrusions

Authors:

Petronis, M.S.[1] (mspetro@gmail.com),

van Wyk de Vries (ben.vanwyk@uca.fr), B[2],

Garza, D (danny.g0629@gmail.com)[1]

[1]Environmental Geology, Natural Resources Management Department, New Mexico Highlands University, Las Vegas, New Mexico, 87701, USA

[2]Université Clermont Auvergne, Observatoire du Physique du Globe de Clermont, Laboratoire Magmas et Volcans, UMR6524-CNRS

The Leaning Puy de Dôme (Auvergne, France) tilted by shallow intrusions

Petronis, M.S.[1], van Wyk de Vries, B[2], Garza, D[1]

[1]Environmental Geology, Natural Resources Management Department, New Mexico Highlands University, Las Vegas, New Mexico, 87701, USA

[2]Université Clermont Auvergne, Observatoire du Physique du Globe de Clermont, Laboratoire Magmas et Volcans, UMR6524-CNRS

Abstract

Acidic lava domes are a special monogenetic volcano type with explosive eruption hazards. Such domes raise questions about the nature of monogenetic volcanism. We study the iconic Puy de Dôme (Chaîne des Puys, Auvergne) that gave its name to 'dome' landforms. It is asymmetric with one side more rugged and steeper than the other. Using mapping and paleomagnetism we find that it was tilted by ~20° south-westwards by bulging from a shallow intrusion, the Petit Puy de Dôme. The Puy de Dôme grew rapidly from this surface-bulging intrusion in one simple pulse, solidified, and was then tilted. During the tilting, there were landslides and the was a final small phreatomagmatic eruption. The dome's history is verging on polygenetic, spanning several hundred years of intrusion and eruption, extending hazard periods. We find other uplifts with paired domes and tilted cones in the Chaîne des Puys and also others in polygenetic systems.

1. INTRODUCTION

Lava domes are a type of volcano with very particular dynamics and hazards (Calder et al., 2015), and monogenetic lava domes are a special class of dome, which by nature of their short, single eruption tend to preserve well any evidence of processes that might otherwise be destroyed by subsequent eruptions in polygenetic volcanoes (Németh, 2010). Such monogenetic volcanoes, while small, can have very complex histories in their short lifespan and they provide useful analogues for larger polygenetic systems (Kereszturi and Németh, 2012, Valentine et al., 2018).

Of equal interest to domes are structures produced by near surface magma intrusion, which are also well preserved in monogenetic volcanic fields (van Wyk de Vries et al 2014), and are found to be common in many settings (e.g. Reeves et al., 2018, Macgee et al, 2017). These structural domes were originally termed 'craters of elevation' (von Buch, 1820), and in structural geology are called 'forced folds' (Cosgrove and Hillier, 1999), or in volcanology the term 'bulges' and 'cryptodome' has been used (Minakami, 1951, Gorshkov, 1959, Moore and Albee, 1981). Bulge is the one term we use mostly in this article, as we are dealing with a surface morphological feature, while we keep in mind that for structural geology we have a forced fold.

Such features are known to have deformed volcanoes, and the magma is known to have broken to the surface and erupted (Minakami, 1951, Macgee et al, 2017). Thus, they are shallow sources of explosive magma, that merit study, as they are obvious harbingers of hazard, and are clearly identifiable as they bulge up. The Usu domes (e.g. Minakami, 1951), probably the most famous polygenetic active shallow intrusion, bulge and dome system is part of a UNESCO Global Geopark, where the cycle of bulging, eruption and recovery is a central theme for risk awareness (Okada 2017, Takarada 2018).

The study of near surface intrusion uplift *and* monogenetic edifice growth provides a combined subject, encompassing the essential question of how volcanoes form and how they erupt, a subject which has been debated since volcanology began. The Puy de Dôme, in the Chaîne des Puys, Central France, is a classic monogenetic volcanic dome, and its name is one of the origins of the term, 'volcanic dome', used since the Puy de Dôme was recognized as a volcano in the mid 18th Century (Guettard, 1752). It has been a focus of volcanological study since this time, as the Chaîne des Puys has continually attracted the attention of scientists by nature of the diversity of volcanic features, its accessibility, and its particular visibility; being raised up on a plateau above the Limagne Rift. This clarity of expression has lead to the 'Chaîne des Puys - Limagne fault Tectonic Arena' being inscribed on the UNESCO World Heritage list in 2018 for rifting-related tectonics and magmatism, such as exemplified by the Puy de Dôme (UNESCO: http://whc.unesco.org/en/list/1434).

The Puy de Dôme has recently been studied for the conditions of dome eruptive dynamics and structure (Maillier et al, 2011, Martel et al., 2015, Portal et al 2016, Boudon et al., 2015, France et al 2016), while it's smaller neighbour the Petit Puy de Dôme, has been studied for intrusion related uplift (van Wyk de Vries et al., 2014). In this latter paper, the authors suggested that the dome grew out of the Petit Puy de Dôme intrusion that created the uplift, however this connection was not studied in detail.

We began to study the Puy de Dôme as, despite this recent attention, detailed knowledge Puy de Dôme's emplacement history through structural mapping and detailed geomorphology was lacking. Also, we were intrigued by the morphology of the dome: like the leaning tower of Piza (also a World Heritage site), the Puy de Dôme has one side steeper than the other, a feature that has attracted the attention of many geologists, and forms the focus of our investigations.

We made use of increased interest in the area as a prospective UNESCO World Heritage site, which promoted more detailed mapping and provided LiDAR data (Openly available on CRAIG – Centre Regional d'Auvergne des Informations Géographiques - https://www.craig.fr/) for the study. The Lidar comes from two data sets, that of the city of Clermont-Ferrand (5 m spacing), and from the LidArvergne campaign at 0.5 m spacing.

Paleomagnetic data are a valuable complement to structural data, with which we expected to provide information on rotations of parts of the dome after cooling. Thus, while mapping the dome we also collected drill core samples for paleomagnetic and anisotropy of magnetic susceptibility analysis (unfortunately this latter AMS data are inconclusive, but are included as an annex for completeness).

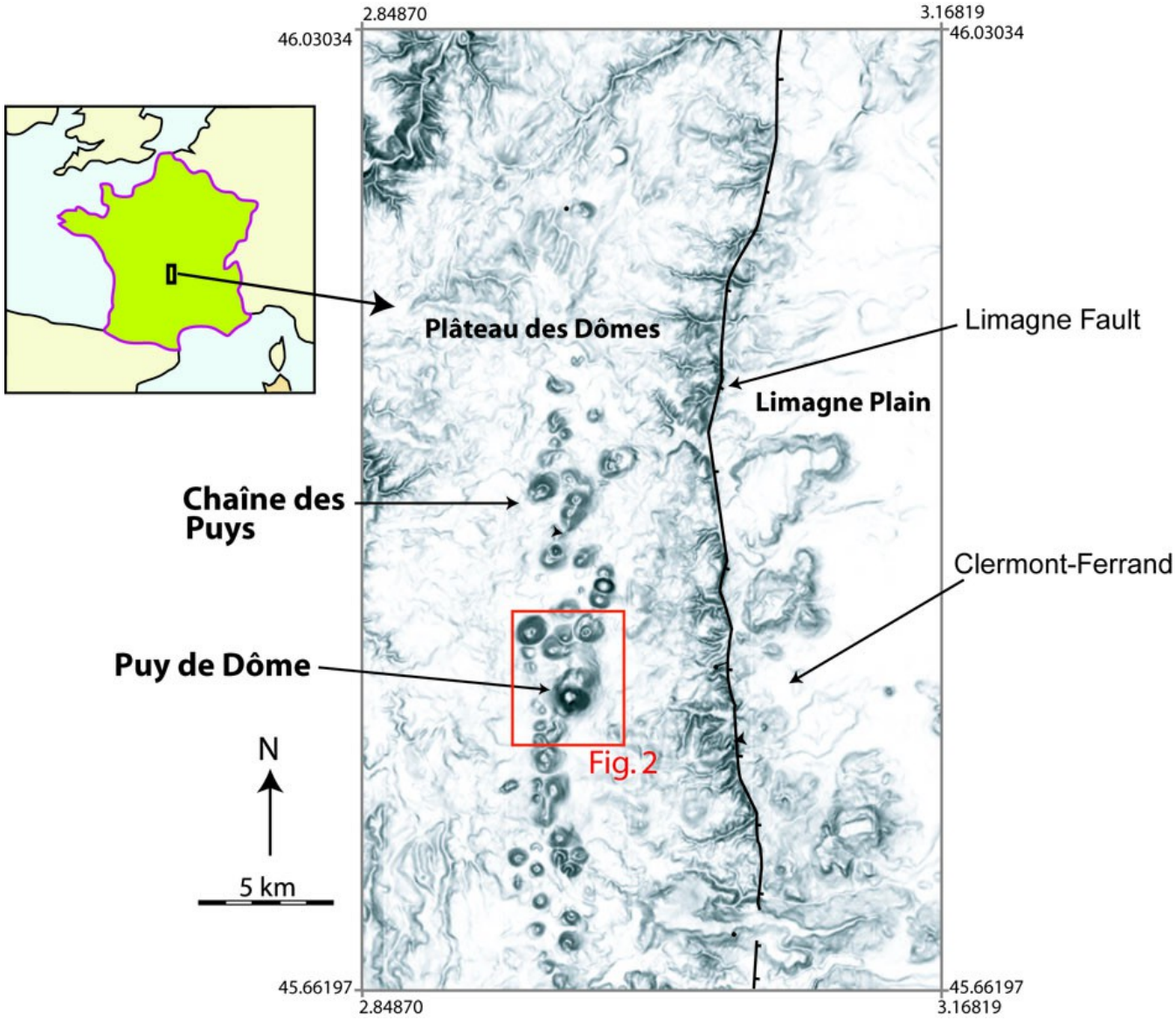

Figure 1. Location map of the Puy de Dôme, set in the Chaîne des Puys, aligned on the shoulder of the Limagne Rift, near Clermont-Ferrand. Their location within France, and the location of the Figure 2 geological map are shown.

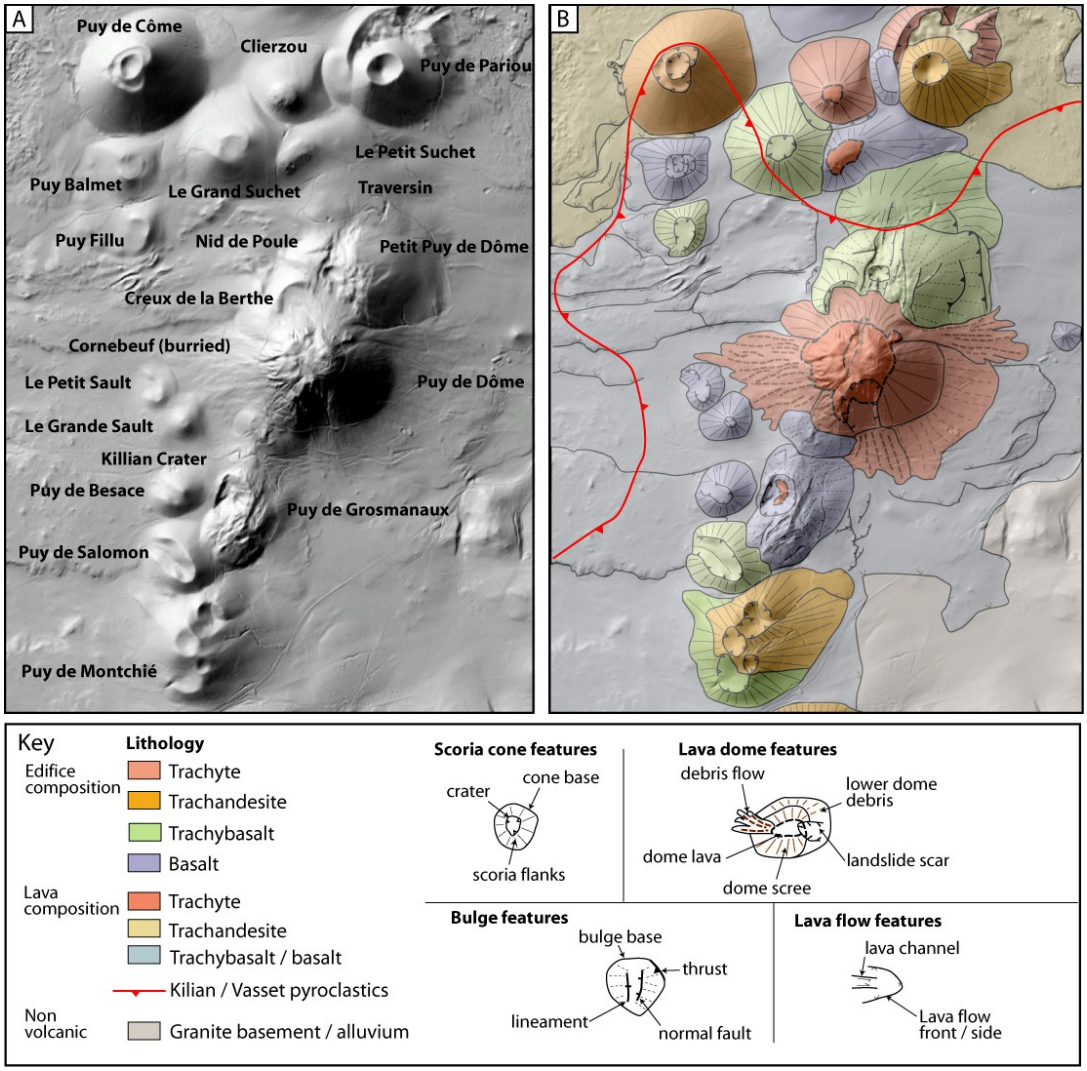

Figure 2. Topography and geology of the Puy de Dôme area. **A)** Shaded relief image using the Lidar data for Clermont-Ferrand (CRAIG dataset). **B)** Geological map, based on the 'Volcanological map of the Chaîne des Puys' (Boivin et al 2017), and our fieldwork (e.g. from van Wyk de Vries et al 2014). The Puy de Dôme is in the centre of the shaded relief image.

While the motivation for this study was initially to study the complexities of the growth of the Puy de Dôme and to compare these observations and data with other domes studied around the world (e.g. Carrasco-Núñez and Riggs 2008, Duffield, et al, 1995; Závada et al 2009), we found quickly that the Puy de Dôme was best understood in context of its surrounding geology and that it was but one part of a prolonged intrusion and eruption event.

We expected from early field work to find evidence of complex rotations of parts of the dome as it grew. However, the paleomagnetic data did not support this hypothesis, suggesting a more simple growth with subsequent slow cooling for the dome itself. In contrast, a complex multistage eruption sequence was uncovered including associated features like the Petit Puy de Dôme, hinted at from earlier work (Maillier et al., 2010, van Wyk de Vries et al., 2014). This activity started before the emplacement of the Puy de Dôme, with uplift and bulging, and it continued after the dome was formed. This late stage activity deformed and tilted the dome, causing faulting and landsliding, and creating its present morphology.

1.1. Description of the Puy de Dôme

The Puy de Dôme is the tallest volcano within the Chaîne des Puys at 1,445 m, and has remained for more tha two milenia an iconic symbol for the region (It had a Gallic and has the remains of a Roman temple on the summit) and is one of the most visited volcanic domes in the world (Jerram et al., 2017).

The Puy de Dôme is about 11,000 years old, and is one of the youngest volcanoes in the Chaîne des Puys (**Figure 1, Figure 2**). The Chaîne des Puys is an ~ 40 km long north-south trending monogenetic alignment of domes, cones, and maars that began erupting about 95,000 ago (Camus et al 1973, Boivin et al 2017). The Chaîne is built on the 'Plateau des Dômes', formed of Hercynian basement and it is parallel to the Limagne fault (**Figure 1)**, which forms the western border of the Limagne rift, part of the larger European Cenozoic Rift System (Merle & Michon, 2001).

The Puy de Dôme is a classic lava dome, with steep sides, a flat top, and a broad breccia apron (see figure 2). Morphologically, it has two distinct sides that have been interpreted as two phases of growth and collapse (Camus et al., 1973, Camus, 1975). On the south and western flanks, the Puy de Dôme is rocky with steep slopes marked by radial ridges, and punctuated by small pinnacles/spine-like points (**Figure 3 to 7**). In contrast, the eastern flank of the Puy de Dôme is smooth and gently sloping and lacks the rugged nature of the south and western flanks (**Figure 3 to 7**).

The north-east side was suggested to have been emplaced into the eastern margin of the first dome after flank collapse (Camus, 1975). Alternatively, it has been suggested that the dome is mostly the product of one eruption, which changed from endogenous to exogenous, covering the initial lava carapace and block and ash deposits with thick cemented ash layers (Boivin et al., 2017).

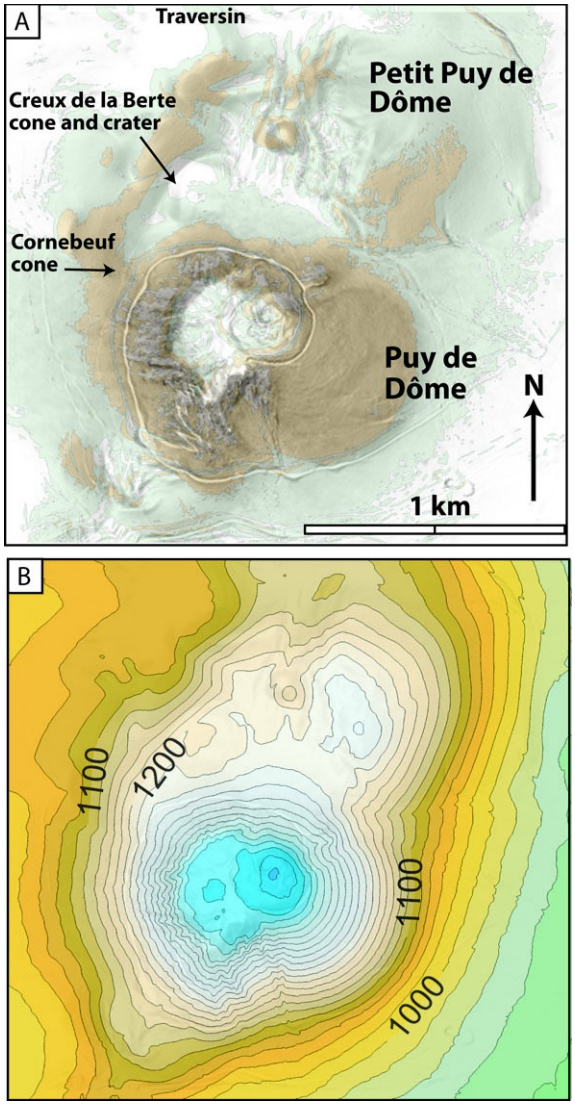

Figure 3: Maps of the Puy de Dôme. **A)** Shaded relief map with transparent slope map overlay. This shows the steepest parts of the Puy de Dôme on the south-west side. **B)** Contour map that shows the steep, closely-spaced crenulated contours on the south-west side, the smooth eastern contours, and the Petit Puy de Dôme bulge to the north-west.

5

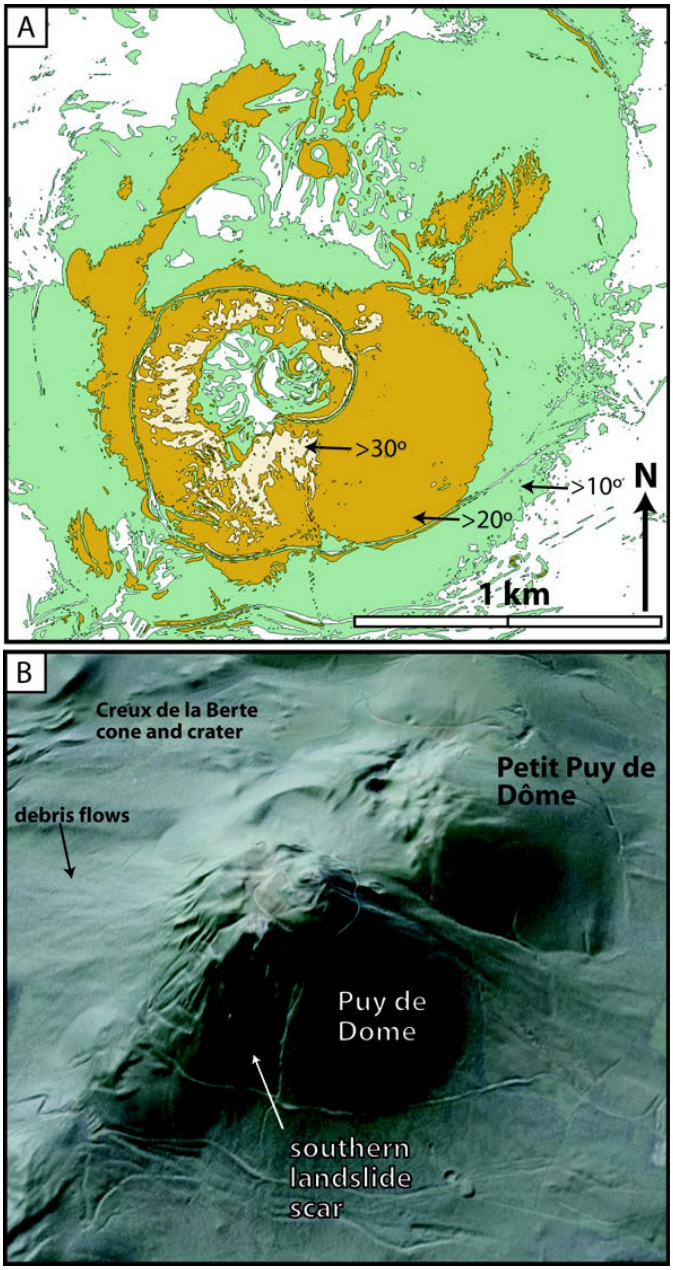

Figure 4. **A)** Slope map (slopes above 20 - Green, 30 - Brown, and 40 - Yellow), showing the concentration of steep slopes on the west and south, while little over 30 in the eastern part. **B)** Oblique image from Google Earth with the Lidar data draped over in transparency. This shows the rugged south-west slopes, the dark, smooth east flank and the Petit Puy de Dôme.

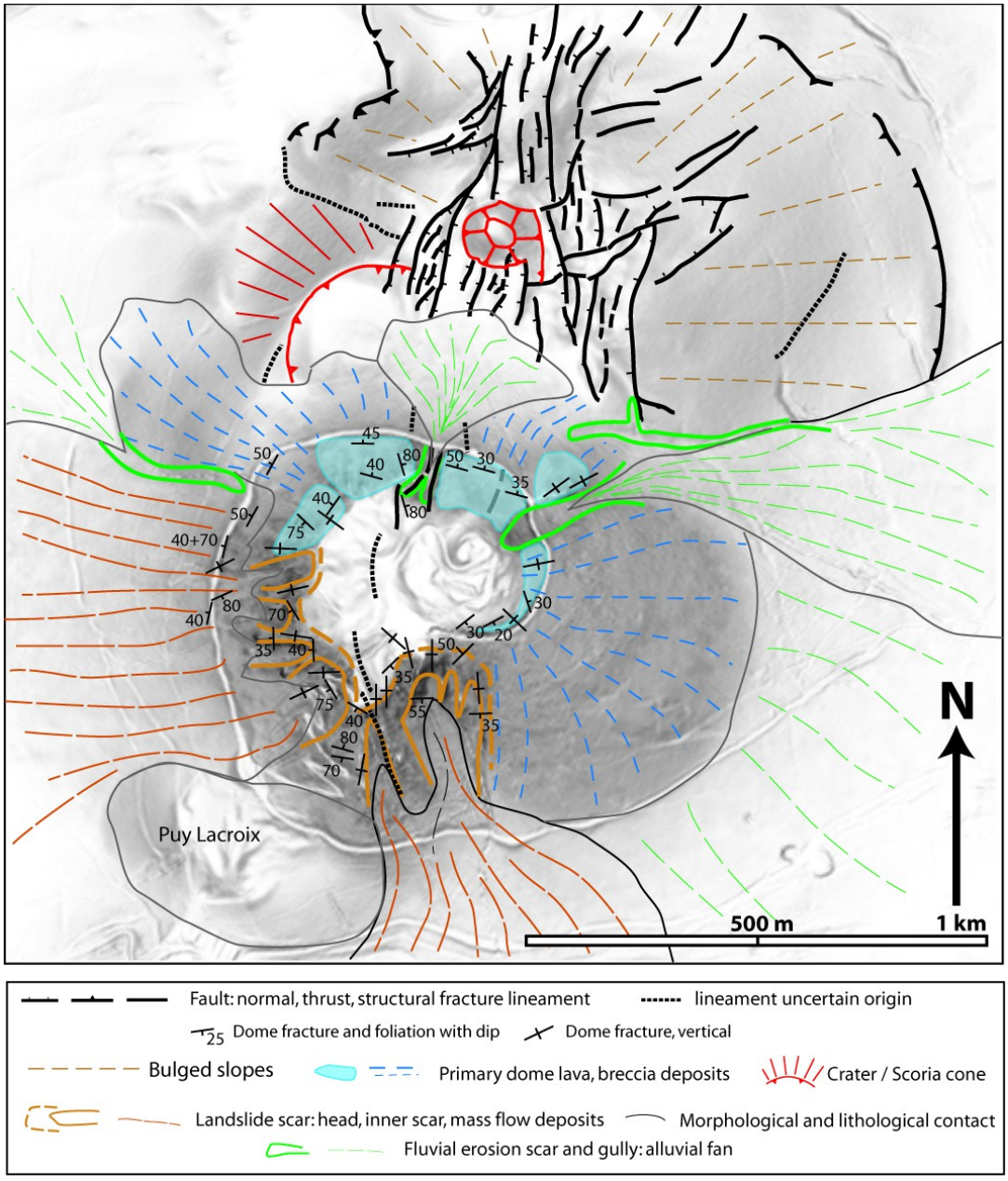

Figure 5. Morphological and structural map of the Puy de Dôme. Note the bulged area of the Petit Puy de Dôme, with its faulted area, and the Nid de la Poule crater inside the main graben. Note also the preponderance of landslide scars and debris flow deposits on the west and south of the Puy de Dôme and their lack on the smooth east side. Fracture and foliation data show two families, concentric down slope foliation, with associated fractures, and radial vertical foliation and fractures. The vertical foliation is mostly seen near the top of the Puy and on the south-west ridge.

The internal structure of the Puy de Dôme has been investigated with electromagnetic, gravity, and muon tomography that have revealed various zones of different degrees of fracturing and/or porosity arranged around a central conduit (Portal et al 2016, Carloganu et al 2013). The dome partially covers possibly two previous scoria cones, seen in the geophysics, called the Creux de la Berte (also visible in the landscape e.g. Figure 5), and another mostly hidden cone called the Cornebeuf (Boivin et al., 2017).

To the north-east of the dome the Petit Puy de Dôme is a prominent bulge formed by 10s to 100s of meters of bulging uplift over a shallow intrusion (van Wyk de Vries et al., 2014). These authors suggested that this bulge pierced the surface at the south-west to form the Puy de Dôme itself.

The eruption age estimates of the Puy de Dôme range from ~12,000 BP to ~9,700 BP based on U-Th age determinations (Condomines, 1997), thermoluminescence dating (Fain et al., 1988; Fain et al., 1991), and radiocarbon dates on peat deposits within and beneath the pyroclastic material (Juvigné and Gewelt, 1987). Most recently, using tephra chronology, Maillier et al. (2010) concluded that the Puy de Dôme was erupted at about 11,000 BP, and may have had two eruptions, the main dome forming event, and a later phreatic event (at about 10,700 BP), before being covered by a vulcanian pumice eruption from the Killian crater 500 m to the south-west at 9,400 BP (Colombier et al 2017).

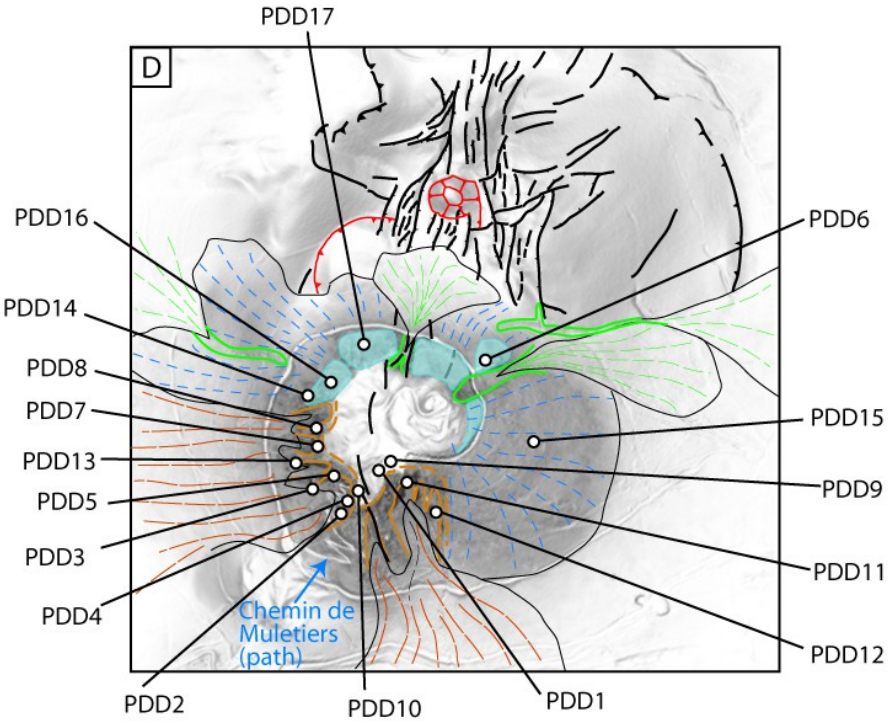

Figure 6: Location of the sample sites, given on the interpretative geomorphological map.

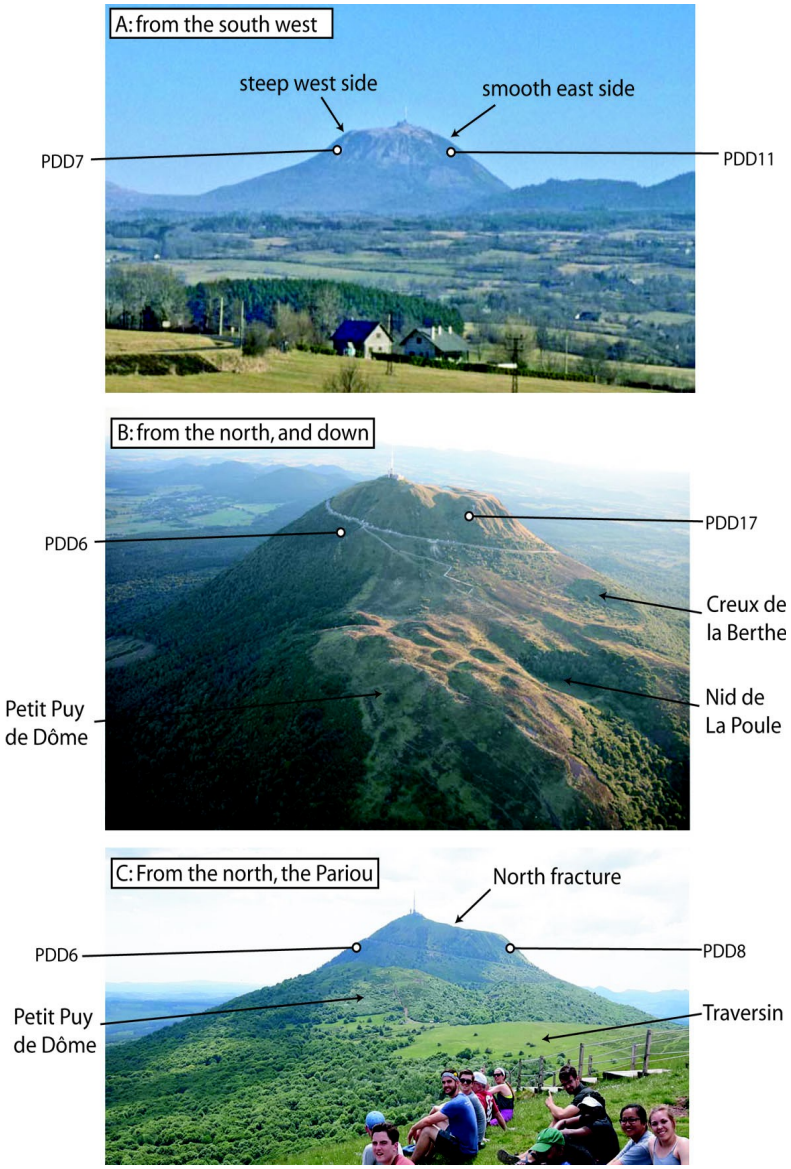

Figure 7. Views of the Puy de Dôme asymmetry from different vantage points, with selected sample points shown. **A)** From the southwest. **B)** Oblique aerial view from the north-northeast, looking over the Petit Puy de Dôme bulge. **C)** From the Pariou volcano summit to the north-northeast, looking past the Petit Puy de Dôme. Location of viewpoints given in Figure 2.

The Puy de Dôme is composed of a greyish trachyte with phenocrysts of potassic oligoclase, sanidine, biotite, and rare green clinopyroxene (Condomines, 1997). Titanomagnetites were the likely initial oxide mineral phase but they have been extensively replaced by hematite (Condomines, 1997). Apatite and zircon crystals are found as inclusions within the feldspar or biotite crystals, and sometimes show epitactic growth (Condomines, 1997).

2. METHODS

2.1. Field work ethics and protocol

The Puy de Dôme is a protected area, and all sampling and fieldwork were carried out with prior permission from the many local landowners and protective bodies. These were the village commune of Ceyssat, who owns the western flanks, the Puy de Dôme 'Grande Site', the local Council of the Puy de Dôme UNESCO World Heritage project, The Puy de Dôme railway and the Regional Park of the Auvergne Volcanoes. Field access was limited to minimise impact on the fragile geosystem and ecosystem of the volcano.

Sampling was done discretely, mostly out of sight of the few paths, with a few holes left visible for educational purposes, as arranged with the UNESCO project. Drill core holes were not filled in, but left to blend into the rock surface, and now form very discrete features that require a keen eye to detect. The return of the sample sites to 'natural' conditions is monitored, and they are at present a subtle mark on rock surfaces (**see Figure 10**), often covered by small plants, and providing niches for small animals.

2.2 Field and Remote Sensing Methods

All sides of the Puy de Dôme were mapped in detail including all the geomorphological and the structural features, such as foliation, fracturing, faulting and alteration. The morphology was also studied using detailed topographic maps and the LiDAR, openly available from the CRAIG data base ('Lidarvergne' data set, https://www.craig.fr/).

Eight to ten drill core samples were collected at each of seventeen sites (**Figure 6 and 10**) across the Puy de Dôme using a modified Echo 280E gasoline powered drill with a non-magnetic diamond tip drill bit. All samples were oriented using a magnetic and, when possible, a sun compass. Drill site locations were precisely located using 62st Garmin GPS.

All core samples were cut into 2.2 cm by 2.5 cm cylinder specimens, using a diamond tipped, non-magnetic saw blade with up to three specimens per core sample obtained at New Mexico Highlands University's Rock Processing laboratory.

2.3 Laboratory Methods

To characterize the magnetic mineralogy, we conducted a suite of laboratory experiments with the goal of identifying the magnetic phases carrying the remanence and anisotropy of magnetic susceptibility fabric (AMS), and the overall ability of these rocks to faithfully record an ambient magnetic field. These data are summarized in **Appendix 1**. Equipment used included an AGICO JR6A dual-speed spinner magnetometer, home-built and ASC Scientific (Model IM-10-30) static

impulse magnets capable of 1 to 3 Tesla peak fields, and a Quantum Design 7 Tesla magnetic properties measurement system. All susceptibility and Curie Point experiments were done with an AGICO MFK1-A kappabridge susceptibility meter with a CS4 high temperature attachment at New Mexico Highlands University Paleomagnetic - Rock Magnetic laboratory.

Rock Magnetic Experiments

Curie point experiments are used to establish the dominant magnetic mineral phase(s) present in the sample and to define the composition of the titanomagnetite phase(s). The samples are heated from the room temperature to 700°C and cooled down at a rate of ~14°C/min in an Argon atmosphere to minimize oxidation of the sample.

To characterize the domain state of the magnetic minerals, we conducted isothermal remanent magnetization (IRM) and low temperature remanence experiments. The IRM acquisition experiments involve progressively magnetizing a sample of near zero initial remanence in progressively higher peak applied fields using an impulse magnet until the specimen reaches saturation. The shape of the IRM acquisition curve provides data on the domain state and magnetic mineralogy.

The low temperature experiments involved field cooled (FC), and zero field cooled (ZFC) experiments with a Quantum Design 7 Tesla magnetic properties measurement system (MPMS). The MPMS experiments are used primarily for magnetic mineral identification based on low-temperature crystallographic transitions (e.g., the Verwey transition; Verwey, 1939), and for characterizing particle size distributions. To evaluate the stability of an induced remanence on cooling and warming, we performed FC and ZFC experiments. The experiment involves the sample being cooled in a sustained DC field of 2.5 T to 10K. The field is then switched off at 10 K and the magnetic remanence is measured as the specimen warms back up to room temperature (FC remanence). The specimen is then subsequently cooled in a null magnetic field (ZFC) to 10 K where a low temperature saturation isothermal remanent magnetization is impart using a 2.5 T applied field, and the remanence is measured again on warming back to room temperature (ZFC remanence).

Paleomagnetic Methods

Remanent magnetizations of all samples were measured using an AGICO JR6A dual-speed spinner magnetometer at the New Mexico Highlands University Paleomagnetic-Rock Magnetic laboratory. Specimens were progressively alternating field (AF) demagnetized, typically in 10 to 25 steps, to a maximum field of 120 mT using a ASC Scientific D-TECH 2000 AF-demagnetizer. Samples with high coercivity were treated with thermal demagnetization (TH) up to a maximum of 630°C, yet with most samples being fully demagnetized by 580°C. Thermal demagnetization experiments on replicate specimens, to compare with AF behavior, were conducted with an ASC Scientific TD48 thermal demagnetizer. Principal component analysis (PCA; Kirschvink, 1980) was used to determine the best-fit line through selected demagnetization data points for each sample using Remasoft 3.0 (Chadima and Hrouda, 2006) (**Figure 10; Table 1**). For most samples, a single best-fit line could be fit to the demagnetization data points. Best-fit magnetization vectors involved 5 to 18 data points, but as

few as 3 to as many as 25 were used, and for less than 10% of the samples it was necessary to anchor them to the origin. Magnetization vectors with maximum angular deviation values greater than 5° were not included in site mean calculations.

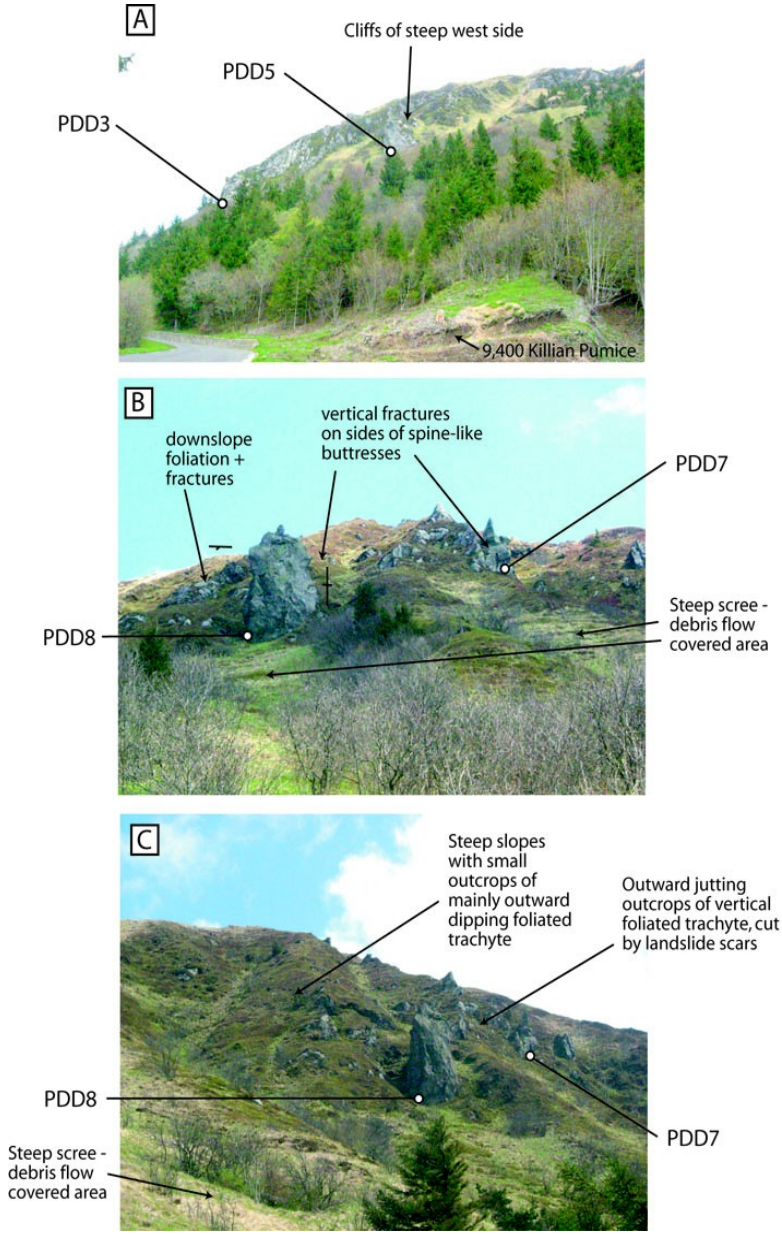

Figure 8. Pictures from the Puy de Dôme, of its slopes. **A)** Looking over the old road (now train track) from the southwest side up to the west side and sample points PDD3 and PDD5. The former forms a large cliff buttress (**Fig. 8b**) with fractures above and below the sampling site that retains a highly fractured down-slope dipping plane. The outcrops above could be an

arrested or potential landslide. **B)** Sample sites PDD7 and PDD 8 on the west side of the steepest part. These are separated by deep landslide gullies. **C**) Same sample sites as B, but viewed from the northwest side.

3. RESULTS

3.1 Field and Topographic Mapping Results

The Puy de Dôme summit has low slopes, cut by small north-south trending scarps, and these flatter areas have been much modified by anthropogenic activity. In contrast, the steeper slopes retain the natural structural and morphological features. The summit plateau has one high peak, which hosts a telecommunication antenna, the Observatoire de Physique du Globe de Clermont-Ferrand's (OPGC) meteorological observatory, and the ruins of a Roman temple of Mercury. Around this peak, there are outcrops of dome lava with dome breccia at the base. The breccia descends down the flanks to the base of the dome. The Killian vulcanian deposits (Colombier et al 2017), which erupted just after the Puy de Dôme, are found in patches on the lower slopes, the summit, and in hollows (Maillier et al 2010, 2012).

On the eastern and northern slopes, the flanks are smooth, cut only by one pinnacle/spine-like feature of dome lava (**Figure 3, 4, 5 and 6**), and there are some narrow, deep erosional gullies from ephemeral streams that activate only during very strong rainfall (**Figure 5**). The gullies open onto alluvial fans, and these reworked slopes pass over a few hundreds of meters onto pre-Puy de Dôme lavas and tephra (**Figure 2 and 6**).

Only one outcrop on the mid eastern flank (PDD15) was large enough to be considered as in place and was sampled. However, good outcrop on the road shows the flank underlain by outward dipping foliated and fractured trachyte.

The southern and eastern slopes of the dome are very different. Starting at the north-east, the dome lava outcrops are cut by a series of deep scars, leaving intervening ridges (**Figure 5 and 8**). The internal layering of the dome is uncovered, exposing down-slope dipping concentric foliation, and fractures with also vertical - steep radial fractures (**Figure 9, and 10**). The trachyte in most outcrops is compact, sometimes crumbly, and the fractures are planes, with often conjugate arrangements. The best exposures of this are seen on the road to the summit (Figure 9C), where cuttings expose a 10's cm spaced conjugate fracture set, the in places has cm-spaced fractures, that form sets of about 60-80° riedel shears, and tension gashes between 20-30° main fractures. The mass remains compact, so the structures formed probably when the rock was near the brittle – ductile transition. There rocks in this area have only the widely spaced vertical fractures that cut the outward dipping foliation.

One particularly sizeable ridge on the south-west side has a series of large down-slope fractures at its base and several large open cracks on its upper side. This is buttressed on its lower edge by a large lava mass, but the freshness of the fractures suggests some continued movement based on the absence of lichen or other vegetation (**Figure 9**).

The landslide scars continue around the dome to the south, interrupted by a large ridge where the main hiking path (Chemin des Muletiers) (**Figure 5**) ascends to the summit. On this ridged area, the dome lava is more massive and the marked down-

slope foliation is more spaced and much steeper (60 – 80°). On this ridge, instead radial foliation and fractures dominate with breccia zones and fumarole-altered outcrops. The vertical foliation creates a serrated morphology. The top of this area flattens and is separated from the summit by a small scarp, which is tentatively interpreted as a slumped block (between sample sites PDD1 and PDD10 on **Figure 5, and see Figure 6**).

To the eastern side of the large ridge, a broad landslide scar occupies the southern flank (**Figure 5**), before the primary smooth eastern slope of the dome is regained to the south-east. The foliation is again concentric and down-slope within and on the edge of this scar, with also radial vertical fractures.

Below all the landslide scars, the terrain is rough and large blocks are mixed with a coarse angular breccia of Puy de Dôme lava. The uneven surface is very different from the smooth eastern slopes and the alluvial fans. Small ridges and scarps that strike down-slope along with the coarse breccias indicate that these are debris flow deposits (**Figure 5, Figure 8**). In some places the Puy de Dôme material is covered or mixed with and pumice from the Kilian eruption, indicating that debris flows also occurred after this eruption.

Immediately to the north of the Puy de Dôme, the Petit Puy de Dôme is a prominent feature (**Figure 2, Figure 5 and Figure 7**). This is a deformed and uplifted scoria cone, with a probable trachytic intrusion below, that also caused a small phreatic eruption, the 'Nid de la Poule' (van Wyk de Vries et al., 2014). **Figure 5** shows the Petit Puy de Dôme and the faults that extend off its southern side, which are aligned with a deep gully on the Puy de Dôme, and the scarps on the dome summit (views in **Figure 7**).

To the south-east of the Puy de Dôme, there is another intrusion-related uplift called the Grosmanaux (**Figure 2**), which hosts the Killian vulcanian crater. The Killian uplift is up to 100 m, half that of the north-eastern Petit Puy de Dôme bulge (van Wyk de Vries et al., 2014).

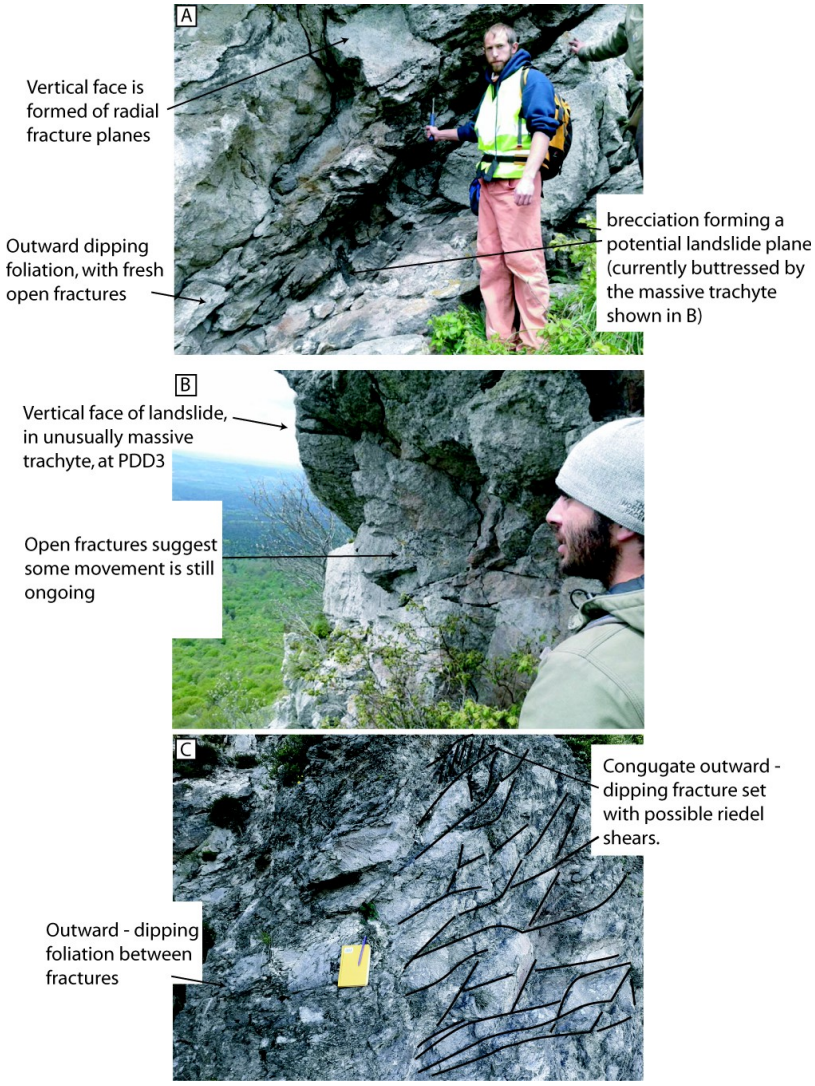

Figure 9. Pictures of the Puy de Dôme outcrops. **A)** Fractured downslope-dipping zone near sample site PDD5. **B)** Massive buttress at PDD3, which is an unusually little foliated or fractured outcrop, that is supporting the landslide planes shown in A. **C**) Outcrop of lava, 200 m down road on south side of Puy de Dôme. Here the trachyte lava shows the typical foliation, and outward-dipping conjugate fractures, with steeper planes as riedel shears. While fractured, the outcrop is one mass, indicating that it deformed while still ductile and hot at low strain rates.

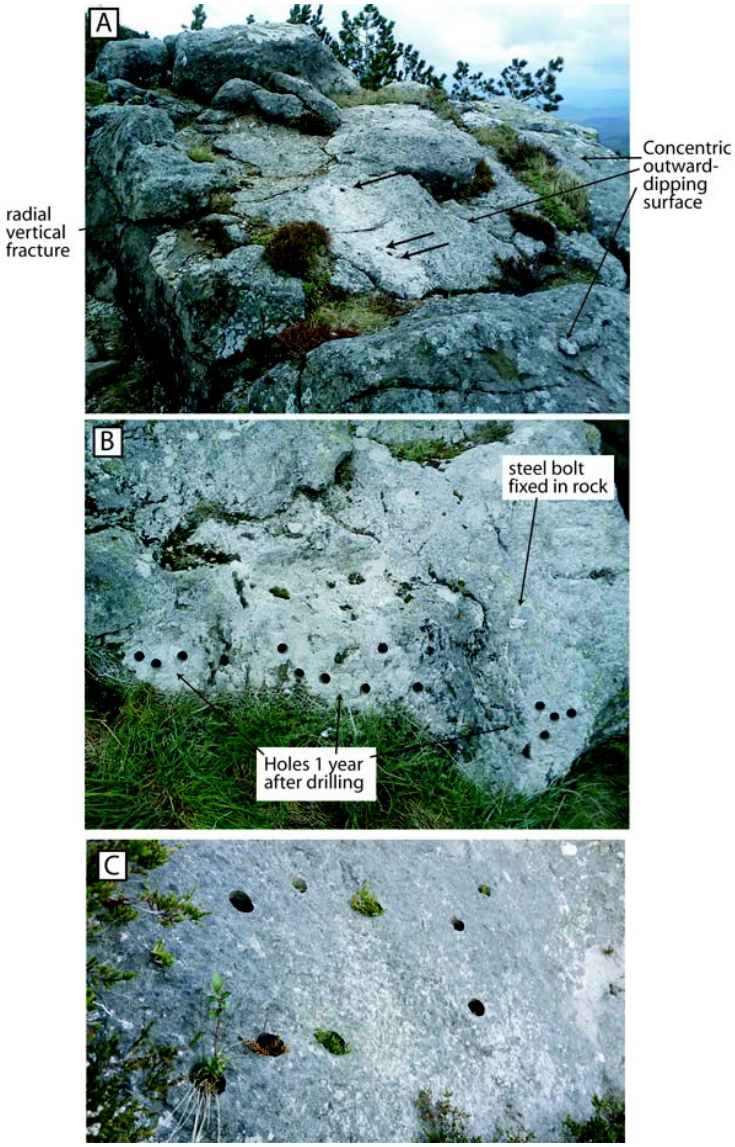

Figure 10. Pictures of sample sites showing how they are integrating back into the natural environment. All sites were chosen to be out of sight of the main tourist paths, in off-limits areas. The exception is for a site near the restaurant terrace, where hole were drilled to be viewed by visitors. Holes were not filled-in, as they return to a 'natural' weathered state better with the least intervention. **A)** PDD9, Just below the summit of the Puy de Dôme on scarp above a slight depression that might be a slumped block. **B)** PDD1 on the very summit of the Puy de Dôme, next to the terrace on the café (note steel ring on rock). **C)** PDD4 on the north of the Chemin des Muletiers, the main walking path up the south-east of the Puy de Dôme.

3.2 Rock Magnetic Experiment Results

Rock magnetic experiments were conducted to determine the magnetic mineralogy and domain state of the principle magnetization carriers in the Puy de Dôme. The rock magnetic data indicate that the dominant magnetic mineral phase is a cubic Fe-Ti oxide of a restricted magnetic grain size, primarily pseudo-single domain titanomagnetite with a minor amount of coarse-grained maghemite and hematite. The detailed rock magnetic results are presented in **Appendix 1**.

Curie Point Estimates

The Curie Point estimates are indicative of a single magnetic phase for most samples of a low to moderate titanomagnetite composition. We do not see evidence of high coercivity phase(s). These data provide evidence that the samples contain a magnetic phase that is capable of preserving a geologically stable magnetic phase capable of preserving a primary remenant magnetization.

Isothermal Remanent Magnetization

All Isothermal Remanent Magnetization *(*IRM) acquisition curves are steep and reach ~ 85% saturation by ~0.40 T with the remaining 15% of the magnetization acquired up to 2.5 T. The results indicate a dominance of magnetite, likely single domain titanomagnetite of a restricted grain size, along with the presence of titanomaghemite and hematite (Özdemir and Dunlop, 1993). These data support the Curie point estimates in that the rocks contain a magnetic phase capable of preserving a geological stable remanence.

Low Temperature Remanence

The magnetic properties measurement system (MPMS) results yield similar curves on warming yet the absolute intensity of the magnetization remanence varies between the three representative samples. All show a suppressed Verwey transition (Verwey, 1939) indicative of non stoichiometric behavior. Ti cation substitution or partial oxidation can lower the transition temperature or suppress it entirely (Özdemir et al., 1993). We see evidence of a hematite Morin transition.

In summary, all the rock magnetic data indicate that the Puy de Dôme trachyte is a material that is capable of preserving a geologically stable remanence and there is no evidence of secondary magnetizations acquired after initial cooling. The remanence is likely to be a primary thermoremenant magnetization (TRM) that was acquired shortly after magma emplacement that formed the lava dome.

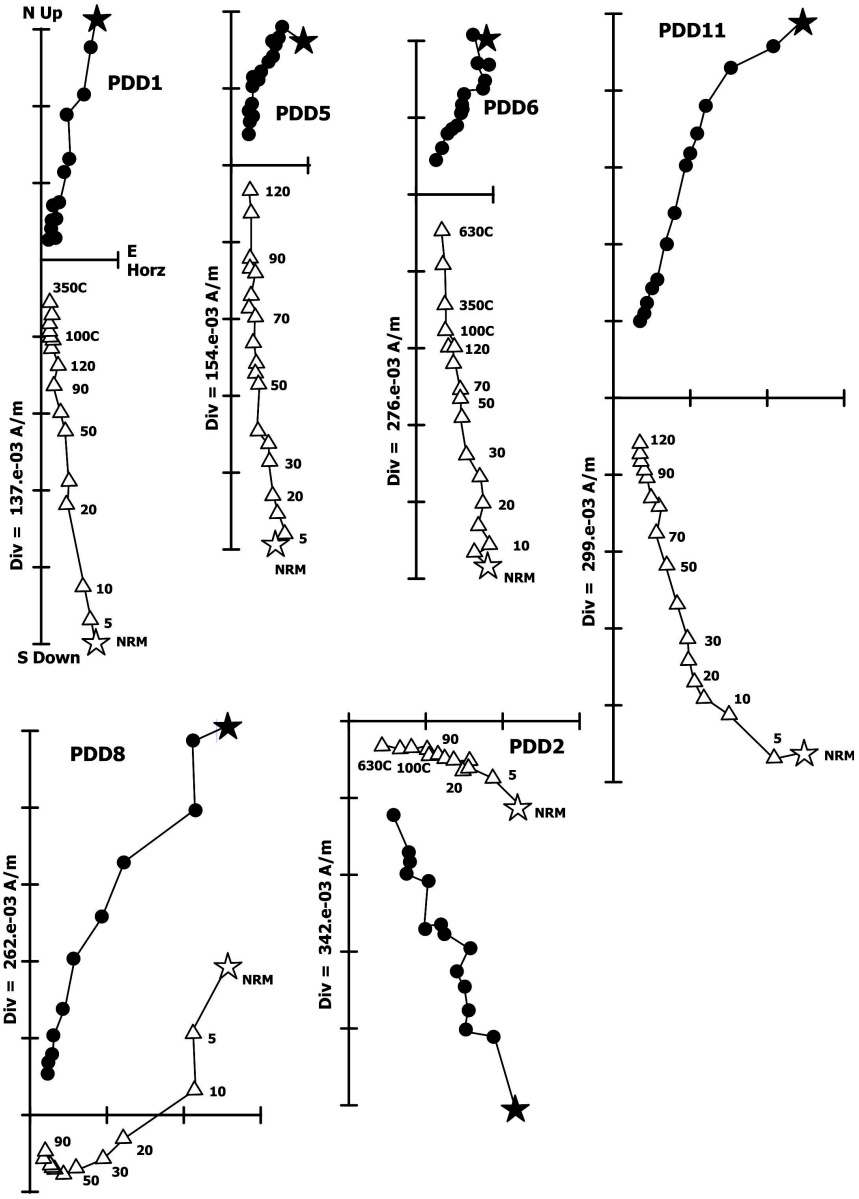

Figure 11: Orthogonal demagnetization diagrams representing the typical AF and TH demagnetization behavior (Zijderveld, 1967). Solid (open) symbols represent the projection onto the horizontal (vertical) plane. The demagnetization steps are given in mT and temperature (T°C). Magnetization (in A/m) is shown along one axis for each sample; each division equals indicated intensity. A few samples contained additional low coercivity viscous remanent magnetization (VRM) components that were readily randomized by 20 mT.

3.3 Paleomagnetic Results

3.3.1 General Demagnetization Behavior

Paleomagnetic data were obtained from seventeen sites across the Puy de Dôme (**Figure 6**). The seventeen sample sites yield overall normal polarity demagnetization results with a few specimens from some sites yielding reverse polarity directional data (**Table 1; Figure 11**). The overall progressive alternating field (AF) demagnetization response is characterized by a near linear trend to the origin for most samples defined over a broad range of peak fields. Most samples yield a single-component magnetization that decayed linearly to the origin with less than 10% of the natural remanent magnetization (NRM) remaining after treatment in 80-120 mT applied field or, for high coercivity phases, treatment with thermal demagnetization up to 630ºC. A few samples contained additional low coercivity viscous remanent magnetization (VRM) components that were readily randomized by 20 mT (**Figure 11**) with the remaining magnetization decaying along a linear trend to the origin.

Table 1: Paleomagnetic data from the Puy de Dôme, Auvergne, France. Explanation: Site, site name; N/No, number of specimens means used in site mean (N) to total number of specimen means at the section (No); Dec/Inc, site declination and inclination; R, resultant vector length; *k*, best estimate of (Fisher) precision parameter; α_{95}, 95% confidence interval of the estimated site mean direction assuming a circular distribution; VGP Lat/Long, latitude and longitude of the virtual geomagnetic pole; Rotation (*R*) and flattening (*F*) and associated error estimates (*+/-R, +/-F*) after Beck, 1980; Demarest, 1983 with respect to the average Quaternary expected field direction.

Table 1: Paleomagnetic data from the Puy de Dome, Auvergne, France

Site	N/No	Dec	Inc	R	α_{95}	*k*	VGP Lat	Long	Rotation R	Error ΔR	Flattening F	Error ΔF	Comments
PDD1	11/12	9.2	70.4	10.7	8.2	32.0	79.3	32.7	9.9	26.6	-6.2	9.2	
PDD2	8/10	359.3	70.4	7.7	10.9	26.9	80.9	0.1	0.0	35.4	-6.2	11.7	
PDD3	6/9	32.1	67.7	5.9	8.8	58.5	68.1	67.5	32.8	25.3	-3.5	9.8	
PDD4	8/8	16.8	76.4	7.9	6.5	74.3	69.1	23.5	17.5	30.1	-12.2	7.7	
PDD5	9/11	18.9	72.8	9.0	3.1	273.7	72.9	38.3	19.6	13.7	-8.6	5.2	
PDD6	9/10	29.1	71.5	9.0	2.2	527.6	68.9	51.6	29.8	11.2	-7.3	4.7	
PDD7	11/11	10.3	75.5	10.8	6.7	46.9	71.9	18.1	11.0	29.2	-11.3	7.9	
PDD8	6/7	16.4	31.4	5.6	20.8	11.4	58.3	151.8	17.1	25.4	32.8	22.1	reject
PDD9	10/10	40.5	17.0	7.5	30.2	3.5	39.4	126.6	41.2	32.3	47.2	31.7	reject
PDD10	5/7	27.4	70.0	5.0	4.4	299.0	70.5	57.2	28.1	15.6	-5.8	6.1	
PDD11	12/12	22.0	70.4	11.9	4.0	116.3	73.3	51.9	22.7	14.8	-6.2	5.8	
PDD12	5/7	24.1	66.1	4.7	20.1	15.4	73.4	73.9	24.8	58.6	-1.9	20.6	reject
PDD13	5/8	26.8	63.1	4.8	17.5	20.0	71.1	86.1	27.5	42.5	1.1	18.0	
PDD14	5/6	38.3	65.9	4.9	10.1	58.2	63.9	73.0	39.0	26.8	-1.7	11.0	
PDD15	9/10	58.9	84.8	8.4	14.5	13.5	50.0	16.6	59.6	-	-20.6	15.0	
PDD16	6/9	31.3	74.6	5.6	19.0	13.3	66.0	40.9	32.0	-	-10.4	19.4	reject
PDD17	8/12	358.9	55.0	7.5	15.7	13.4	80.0	188.0	0.6	29.2	9.2	16.4	

Table 2: Quaternary virtual paleomagnetic pole positions and calculated expected directions for the Puy de Dôme.

Explanation: Rock Name; Age, estimated age in millions of years (Ma) or thousands of years (Ka); VGP Position, virtual geomagnetic pole position; Expected Direction , based on the cited references; A95 (estimated), error estimate of the calculated pole position; *extracted from the Global Paleomagnetic Database.

Table 2: Quaternary virtual paleomagnetic pole positions and calculated expected directions for the Puy de Dome

	Age	VGP Position			Expected Direction		(estimated)	
Rock Name		**Plat**	**Plong**	**A95**	**Dec**	**Inc**	**A95**	**Reference**
River Volga Sediments, Central Europe	1.0 Ma	81,0	227,0	4,0	347,2	63,8	2,8	McElhinny and Lock (1995)*
Shoshone Ice Caves, ID	10,130 Ka +/-350 Ka	82,8	81,8	2,7	10,3	64,6	1,9	Champion (1980)
Pronghorn Reservior Flows, COM, ID	10,240 Ka +/- 120 Ka	79,3	352,7	1,5	356,7	71,4	0,9	Hagstrum and Champion (2002); Champion (1980)
Horse Caves flows, MLV, CA	~12,700 Ka	70,2	153,4	9,9	10,8	46,4	9,6	Champion and Donnally-Nolan (1994)
Giant Cartor precurcr flows, MLV, CA	10,676 Ka +/- 38 Ka	75,5	335,0	2,8	347,4	72,5	1,7	Champion and Donnally-Nolan (1994)
Valentine Cave basalt flow, MLV, CA	10,850 Ka +/- 60 Ka	78,6	330,1	4,6	349,4	70,5	2,9	Hagstrum and Champion (2002)
Synthetic VGP Poles 10 Myr sliding Window	0 Ma - 10 Ma	86,3	172,0	2,6	0,9	60,8	1,9	Besse and Courtillot (2002)
Synthetic VGP Poles 5 Myr sliding Window	0 Ma - 5 Ma	86,7	178,7	3,0	0,3	61,1	2,2	Besse and Courtillot (2002)
Mean Calculated Expected Direction		89,3	320,9	8,2	***359,3***	***64,2***	***5,7***	

Four sites did not yield stable end-point behaviour or had a high dispersion between specimens within the site (random normal and reverse polarity directions); these four sites were rejected and will not be discussed further. The thirteen accept sites yield well-defined normal polarity magnetization directions that provided a group mean direction of D = 019.7º, I = 70.8º, α_{95} = 4.4º, k = 90.1 n = 13, which is statistically distinct at a 95% confidence level from the expected Quaternary normal polarity field direction (D = 359.3º, I = 64.2º, A_{95} = 5.7º) based on the average data of multiple Quaternary virtual paleomagnetic pole positions (**Table 2; Figure 12)**.

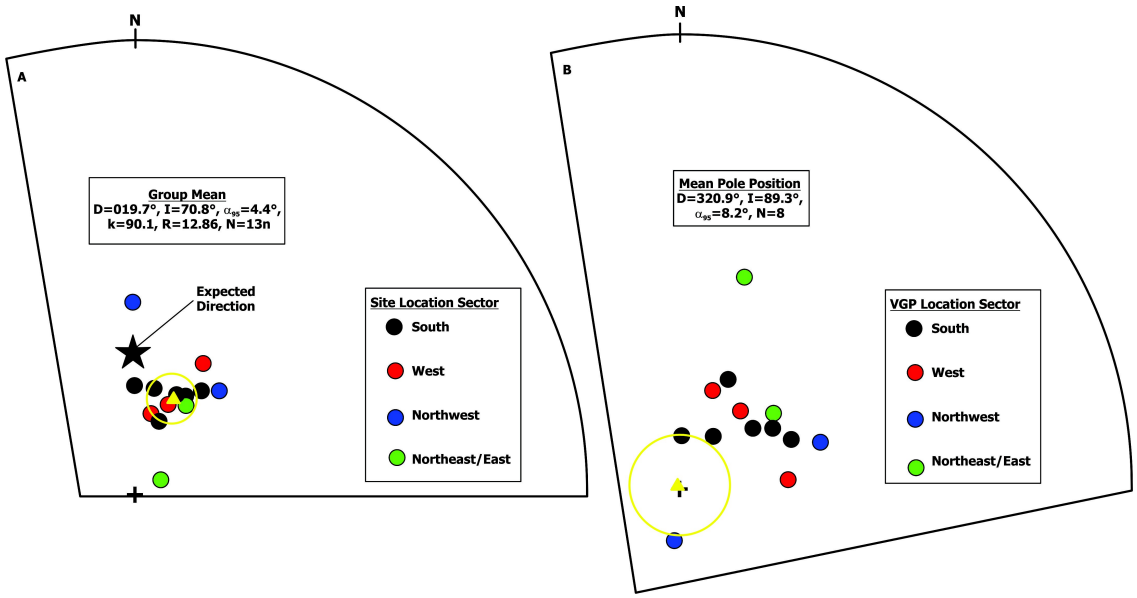

Figure 12: Paleomagnetic data from the Puy de Dôme. **A)** Lower hemisphere equal area projection of site mean paleomagnetic data from the Puy de Dôme. The yellow triangle indicates the group mean result of the 13 accepted sites with α_{95} confidence ellipse about the group mean direction. The black star is the Quaternary reference direction based on the average of multiple paleomagnetic poles (**Table 2**). **B)** Lower hemisphere equal area projection of site mean virtual geomagnetic pole positions (VGPs). The yellow triangle with A_{95} confidence ellipse indicates the mean Quaternary virtual geomagnetic pole position (**Table 2**)

To test the dispersion of the site mean virtual geomagnetic poles (VGPs), we compared the average VGP dispersion to the predicated dispersion value for the latitude of the site (45.5° N) (Merrill and McElhinny, 1983). If secular variation has been adequately sampled, the observed angular dispersion estimate of site mean VGPs should be consistent with that predicted. In

this case ~ 17.0° with a +/- error range of 18.0° to 15.5° (**Table 1;** Merrill and McElhinny, 1983). The estimated dispersion (S) of the thirteen accepted site mean directions yields a group mean VGP dispersion of 13.3° +/- 6.9° (95% confidence); a value which is less than, yet statistically indistinguishable from, the predicted VGP dispersion estimate. From this analysis, we suggest that the thirteen sites may reflect either 1) a time interval covering the longer periodicities of secular variation and represent a time averaged result, or 2) tectonic deformation associated with differential tilting of the dome. As we discuss below, we prefer the latter interpretation of the data given the field relationships.

3.4 Anisotropy of Magnetic Susceptibility Results

Appendix Table 1 summarizes all anisotropy of magnetic susceptibility data and key magnetic parameters. K_m intensities (in the SI system) are moderate and range from 9.81×10^{-3} SI to 0.24×10^{-3} SI with a mean of $3.16\times10^{-3} \pm 2.53 \times10^{-3}$ SI. The AMS fabric results reveal a near random orientation of K_1 lineation and K_1-K_2 foliation plane data; 16 of 17 susceptibility ellipsoid shapes are oblate (**Appendix Table 1; Appendix 1**). The corrected degree of anisotropy (Pj; Jelínek 1981) varies between 1.011 and 1.164, and averages 1.067 ± 0.053, indicating a weak (~ 6%) degree of anisotropy. The magnetic lineation (L) and foliation (F) averaged 1.014 ± 0.015 and 1.048 ± 0.041, respectively. There was no correlation between the corrected degree of anisotropy (Pj) and mean susceptibility (K_m), and no correlation between the shape parameter (T) and K_m, Pj versus T.

4. DISCUSSION

Implications of the Paleomagnetic Data

The paleomagnetic and existing geochronology data from the Puy de Dôme places magma emplacement during the normal-polarity Chron C1n (0.0 Ma-0.780 Ma) in the Holocene (Gradstein et al., 2012). The group mean data are statistically distinguishable at 95% confidence level from the expected Quaternary normal polarity field direction (**Table 2**) and yield a rotation (R) and flattening (F) estimate of R=20.4° +/-12.5° and F=-6.6° +/- 7.5° relative to the expected field direction (**Table 1**).

This paleomagnetic data can be interpreted as being either a time averaged result, a spot reading of the geomagnetic field, or a time-averaged result with the directional discordance attributed to deformation of the dome. The dispersion of the VGPs is less than the predicted value of ~ 17°, but there is statistical overlap. Here, we argue that the paleomagnetic data likely do not represent a time average result and the spatially variable directional data reflects tectonic deformation that has led to the discordance of the data relative to the expected field direction.

In order to evaluate the paleomagnetic data more fully to assess any possible variation in age or true dispersion among the data, a mean discrimination test was conducted between each individual site means (McFadden and Lowes 1981). Essentially, the test compares an observed site mean direction to another observed site mean direction with the null

hypothesis being that the two mean directions are separate samples from the same population of directions and the same geomagnetic field direction. Alternatively, if the means are distinct, they were either drawn from different populations that sampled different geomagnetic field directions or sub-volcanic deformation occurred which increased the dispersion of the data between sampling locations. The mean discrimination test does not prove the null hypothesis, but sets a probability (in this study 95%) of it either being accepted or rejected. The mean discrimination test results reveal that seven sites are statistically distinguishable at the >95% confidence level from the other six accepted sites (**Table 1**). The remaining sites are statistically indistinguishable from each other at >95% confidence.

We interpret the statistically distinct sites to reflect some post-emplacement deformation following remanence acquisition. The pattern of deformation across the dome reveals that the tilting (i.e., rotation) is, for the most part, uniform with only local deformation between a few site locations. We suggest that the subvolcanic deformation from the Petit Puy de Dôme may have caused the observed discordance of the paleomagnetic data following remanence acquisition.

4.1 Emplacement and Deformation Mechanism of the Puy de Dôme

The geomorphological, structural and paleomagnetic data all indicate that the Puy de Dôme has been tilted to the south-east some time after it erupted and cooled. The paleomagnetic data also suggest that the dome extruded as one unit and solidified without any major reorientation of the cooled carapace. This makes the Puy de Dôme a monogenetic dome with one short-lived eruption, but the tilting and activity of the Petit Puy de Dôme began before, and continued until after the simple dome extrusion (**Figure 13 and 14**).

Subsequent to the dome emplacement there was another eruption from the summit, a few hundred years after the cessation of the first (a thin soil is present between the two deposits (Maillier et al 2010)). A thousand years after this, the Killian erupted and its products were deposited over the Puy de Dôme, and during this interval two small trachyandesite eruptions (Nid de la Poule and possibly the Traversin) occurred, as well as the trachyte - basalt Puy de Pariou eruption just to the north-east (Maillier et al 2012). Killian tephra deposits are found on the Petit Puy de Dôme (Maillier et al 2012), so the deformation associated with the latter, and thus the tilting, could extend to around the eruption of the second Puy de Dôme tephra. Since the Petit Puy de Dôme is considered to have triggered the eruptive sequence by growing and then breaching to the south-west to allow the extrusion of the Puy de Dôme, this bulge growth both *pre-dates* and *post-dates* the Puy de Dôme.

The sequence is thus: Petit Puy de Dôme bulging > Puy de Dôme lava extrusion > ongoing growth of Petit Puy de Dôme + final Puy de Dôme small eruption > Nid de la Poule eruption (+ more bulging?) > Killian eruption.

If we draw comparisons with current volcanic activity, the Puy de Dôme – Petit Puy de Dôme growth could be seen as an equivalent of the Usu volcano domes (Minakami et al., 1951; Katsui et al., 1985; Tobita et al., 2001), which grew in a matter of weeks to months. The long term growth of the Petit Puy de Dome could be equated to the continually deforming Alu bulge in Ethiopia (McGee et al 2017, Pagli et al 2012).

Both eruption and tilting of the Puy de Dôme thus probably happened over weeks to months, while the intrusion growth took maybe a few hundred years, possibly extending to the Nid de Poule eruption with a more mafic magma input.

The petrographic and intrusive sequence of events can be seen as a prolonged monogenetic eruption, during a heightened period of activity in the Chaîne des Puys, which verged on polygenetic in its duration and complexity.

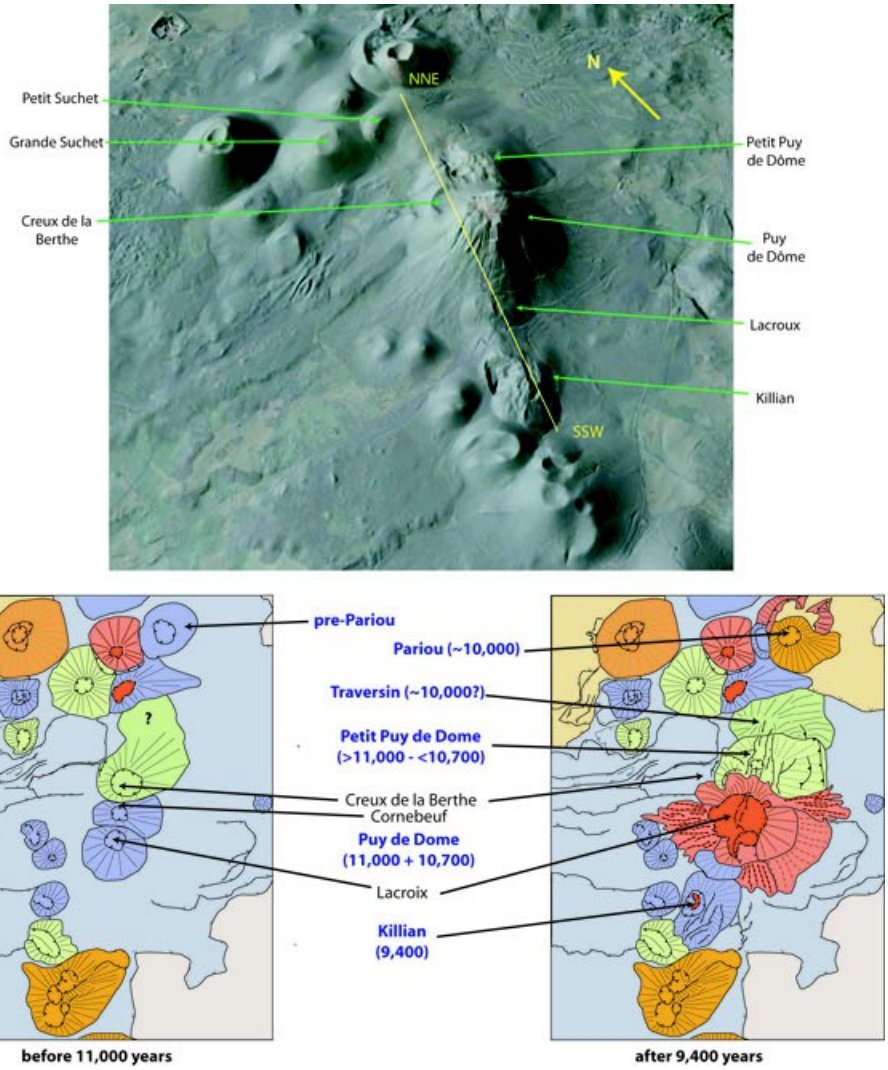

Figure 13. History of the Puy de Dôme area. **A)** Oblique image of LiDAR-derived shaded relief (CRAIG dataset), overlain on the Google Earth image of the Puy de Dôme area. Line of cross section in **Figure 14** shown in yellow. **B)** Map of the area up to 10,000 years before the start of the Petit Puy de Dôme intrusion. **C)** Map after 9,400 years (e.g. like in **Figure 2**), with the newly appeared volcanoes and structures indicated. Compare this diagram with the cross-sections in **Figure 14**.

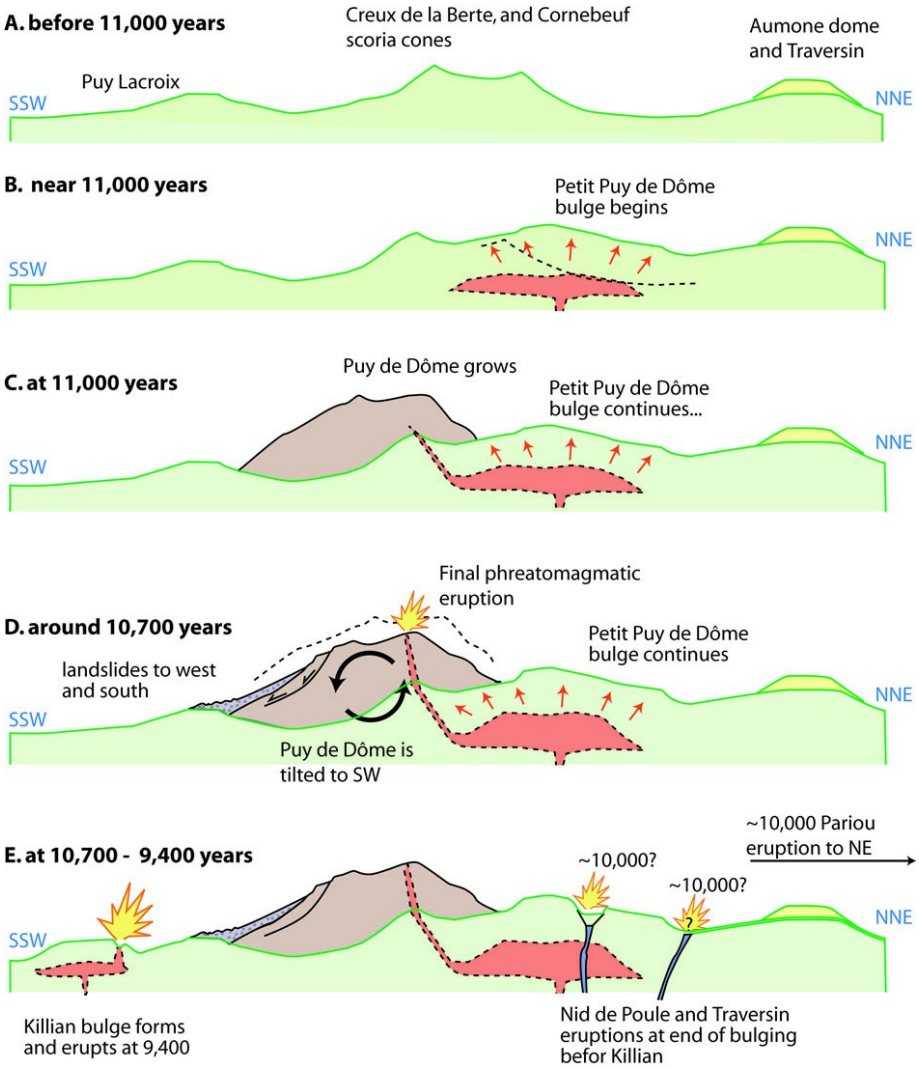

Figure 14: Summary cartoon of the sequence of events around the Puy de Dôme. **A)** Pre-Puy de Dôme before 11,000 years BP. The area is mostly older scoria cones, with one trachyte dome, the Petit Suchet, emplaced a few thousand years before. **B)** Start of activity with shallow intrusion starting to create the Petit Puy de Dôme bulge. **C)** Trachytic magma breaks through on the south of the bulge to allow the Puy de Dôme to grow. The dome gains a carapace of ash towards the end (Boivin et al 2017). **D)** The cooled Puy de Dôme is then tilted by continued growth of the Petit Puy de Dôme, and a small summit eruption occurs around 10,700 BP. **E)** Activity stops, and a small trachyandesitic eruption cuts the Petit Puy de Dôme (Nid de la Poule) and possibly a small vent opens on the Traversin. This activity may have occurred at about 10,000 years with the Pariou eruption. Then at 9,400 BP the whole area is covered by Kilian eruption deposits.

The Puy de Dôme is not the only volcano in the Chaîne des Puys to have been affected by subsequent, geographically-close eruptions. For example, the Grand Suchet is tilted to the west by the Puy Suchet trachyte intrusion (van Wyk de Vries et al., 2014). Also, the Chopine trachyte intrusion deformed the Puy de Gouttes before destroying the latter in a sector collapse (van Wyk de Vries et al., 2014). Other cones, such as the Montchie and Lemptégy have had multiple eruptions (Petronis et al., 2013; Maillier et al., 2013), separated by long time-periods during which the edifices have completely cooled. An extended sequence is also seen with the Pariou eruption and that of the Puy de la Nugère (Camus et al 1973, Boivin et al 2017), that go from initial trachyte to basalt.

The response of each cone to the subsequent intrusion/eruption varies. In general they all are deformed and tilted, and may additionally be pierced by eruptions and/or suffer landslides. The Puy de Dôme itself has been tilted, pierced by a small eruption and has undergone a landslide on the south-west side. The reason that there was not a larger collapse, such as that of the Gouttes, might relate to the strength and structure of the Puy de Dôme trachyte, which ensured that the core remained intact while only some of its outer carapace was shed on the outward-dipping planes.

As many cones in the Chaîne des Puys have been affected by subsequent tilting, such activity might be related to the dense concentration of edifices; the Chaîne has the highest concentration of any monogenetic field (Le Corvec et al 2013). Such interference between edifices would be less likely in more spread out monogenetic fields. On stratovolcanoes, pulses of magma intrusion follow one after another, and so similar tilting could occur. However, the magma volume may be small with respect to the volume of the edifice, creating a partial bulge rather than tilting, such as at Mount Saint Helens or Bezymmianny (van Wyk de Vries et al 2014). Larger intrusions might occur, but the likelihood of magma breaking out at the surface might limit the scale of uplift and tilting, instead giving rise to the formation of a satellite cone. Also the larger size of a stratovolcano with respect to its internal strength would favour deformation of a relatively smaller area. Thus tilting of an entire, large stratovolcano seems unlikely, at least by shallow intrusions, but growth of larger magma chambers at greater depths could provide the volume and area of uplift to tilt a large volcano. The large-scale sliding of the Mull volcano (Mathieu et al 2009), or the present-day Mount Etna could be considered in this context. The huge uplift and sliding identified at Heart Mountain, Utah (Beutner and Gerbi 2005) shows that such grand-scale tilting is possible. So finally, while it appears most likely that tilting is more common on small, monogenetic volcanoes, especially lava domes, the same processes can occur in a scaled up way in larger systems.

The message for monitoring and hazards is that broad uplift beneath one side of a volcano might be accompanied by a collapse of the opposite side, in the direction possibly least expected.

The paired opposite collapses at Mombacho, Nicaragua, might be an example of this (Shea et al 2007), where intrusion and alteration of a bulge on the SE side caused a landslide on this south side, as well as generating a corresponding slide on the north side. Therefore, when volcanoes start to deform due to an intrusion, a whole range of possible scenarios need to be considered. It is only with continued growth of such a bulge that the outcome might become clear.

5. CONCLUSIONS

Geomorphological mapping has showed that the Puy de Dôme is asymmetric and steeper to the south-west than the north-east. Paleomagnetic data are consistent with a modest tilt of the dome on a north-west axis. The tilt is best explained by the 200 meters of uplift produced on the north-east side by the Petit Puy de Dôme bulge. The low dispersion of the paleomagnetic data from the Puy de Dôme also suggests that the dome cooled essentially *en-masse* without significant post eruption flow.

Whole-scale tilting of volcanoes by intrusions may have occurred at other volcanoes in the Chaîne des Puys and elsewhere. At larger scales this could affect the stability of large stratovolcanoes.

Precursory activity, in terms of doming and faulting at the base of the edifice could provide timely warning of the way intrusions are developing. Such activity is especially likely to occur at previously dormant volcanoes that have consolidated their conduits. Deformation on one side might cause landslides on the other side, where it might not be expected. Hazard assessment should take this into account in the event of an intrusion being detected, as the opposite side from the most obvious danger may be at risk.

The tell-tale signs should be seen in tilting of the edifice away from a peripheral uplift, displacing the whole volcano to one side. Fracturing and precursory sliding on the opposite side of a bulge could also be a precursor to larger instability.

6. ACKNOWLEDGEMENTS

This work was funded by New Mexico Highlands University Faculty Research funds, National Geographic Grant #8887-11 awarded to Petronis and Lindline, National Science Foundation Grant #1423396 awarded to Petronis and Lindline, and National Science Foundation Grant DMR-1523611 (PREM) awarded to Tatiana Timofeeva.. A special thanks to Dr. Linda LaGrange for her support of faculty and student research at New Mexico Highlands University. This work represents a large portion of Mr. D. Garcia's masters thesis research at New Mexico Highlands University. Both Petronis and van Wyk de Vries were primarily responsible for drafting the figures, data interpretation, and content of the manuscript. All data related to this project will be made available at http://www.nmhugeology.com/, the paleomagnetic data will be uploaded to the MagIC database (https://www2.earthref.org/MagIC), and all data sets may be requested from the author (mspetro@nmhu.edu). A very special thank you to F. van Wyk de Vries for editing the manuscript. Tatum Miko Herrero, Giachino Roberti assisted with the field sampling. Permission of sampling came from the Grande Site du Puy de Dôme, the Conseil Departmental du Puy de Dôme and the Train du Puy de Dôme as well as the commune of Ceyssat. The final work has been carried out under the UNESCO Geosciences Project No 692 'Geoheritage for Geohazard Resilience'

7. REFERENCES

Akimoto, S. 1962, Magnetic properties of FeO/1bFe2O3/1bTiO2 system as a basis of rock magnetism. J., Phys. Soc. Jpn, 17 (suppl. B-1) (1962), p. 70 C.

Beck, M.E., 1980, Paleomagnetic record of plate-margin tectonic processes along the western edge of North America: Journal of Geophysical Research, v. 85, p. 7115–7131, doi: 10.1029/JB085iB12p07115.

Besse, J., Courtillot, V., 2002. Apparent and true polar wander and the geometry of the geomagnetic field over the last 200 Myr. J Geophys Res: Solid Earth 107: 6–31

Beutner, E.C., Gerbi, G.P., 2005 Catastrophic emplacement of the Heart Mountain block slide, Wyoming and Montana, USA, Geological Society of America Bulletin 117(5). DOI: 10.1130/B25451.1

Boudon, G., Balcone-Boissard, H., Villemant, B., Morgan, D.J., (2015) What factors control superficial lava dome explosivity? Scientific Reports volume 5, Article number: 14551

Boivin, P., Besson, J.C., Briot, D., Camus, G., De Goër de Hervé, A., Gourgaud, A., Labazuy, P., Langlois, E., de Larouzière, F.D., Livet, M., Mergoil, J., Miallier, D., Morel, J.M., Vernet, G., Vincent, P.M., 2017. Volcanologie de la Chaîne des Puys Massif Central Français, 5th Edition, scale 1:25 000, 1 sheet

Calder, S., Lavallée, T., Kendrick, E., Bernstain, M., (2015) Lava Dome Eruptions, Ch 18 The Encyclopedia of Volcanoes (Second Edition), 2015, Pages 343-362

Camus, G., de Goër de Hervé, A., Keiffer, G., Mergoil, J., Vincent, P.M., 1983. Volcanologie de la chaine des Puys (Massif Central Français). Map explication booklet 2nd edition. Parc Naturel Regional des Volcans d'Auvergne, découverte de la nature, v. 8, P112.

Camus, G., 1975, La Chaîne des Puys (Massif Central, Francais): Etude structural et volcanologique. Doctoral Thesis. University of Clermont-Ferand, France.

Cârloganu, C., Niess V., Béné, S., Busato, E., Dupieux, P., Fehr, F., Gay, P., Miallier, D., Vulpescu, B., Boivin, P., Combaret, C., Labazuy, P., Laktineth, I., Lénat, J.F., Mirabito, L., Portal, A., 2013, Towards a muon radiography of the Puy de Dôme, Geoscience Instrumental and Methodological Data systems, 2, 55-60.

Carrasco-Núñez, G. & Riggs, N., 2008. Polygenetic nature of a rhyolitic dome and implications for hazard assessment: Cerro Pizarro volcano, Mexico. Journal of Volcanology and Geothermal Research, Volume 171, pp. 307-315.

Chadima, M. and Hrouda, F. 2006. Remasoft 3.0 – a user-friendly paleomagnetic data browser and analyzer. Travaux Géophysiques, XXVII, 20–21.

Colombier, M., Gurioli, L., Druitt, T., Shea, T., Boivin, P., Miallier, D., Cluzel, N., 2017. Textural evolution of magma during the 9.4-ka trachytic explosive eruption at Kilian Volcano, Chaîne des Puys, France. Bulletin of Volcanology vol.79, p.17, doi:10.1007/s00445-017-1099-7.

Condomines, M., 1997., Dating recent volcanic rocks through 230T-238U disquilibrium in accessory minerlas: Example of the Puy de Dôme (French Massif Central), Geology, Volume 25, pp. 357-378.

Cosgrove JW, Hillier RD (1999), Forced-fold development within Tertiary sediments of the Alba Field, UKCS: evidence of differential compaction and post-depositional sandstone remobilization: Geol Soc Lond Spec Pubs, 169(1): 61-71

De Wall, H., 2000, The Field-Dependence of AC Susceptibility in Titanomagnetites: Implications for the Anisotropy of Magnetic Susceptibility. Geophysical Research Letters, 27(16), 2409–2411.

Demarest, H.H., 1983, Error analysis of the determination of tectonic rotation from paleomagnetic data: Journal of Geophysical Research, v. 88, p. 4321–4328, doi: 10.1029 /JB088iB05p04321.

Duffield, W. A., Richter, D. H. & Priest, S. S., 1995. Physical volcanology of silicic lava domes as exemplified by the Taylor Creek Rhyolite, Catron and Sierra Counties, New Mexico, s.l.: U.S. Geological Society.

Dunlop, D.J., and Özdemir, Ö., 1997. Rock Magnetism: Fundamentals and Frontiers. Cambridge University Press, New York, London, and Cambridge, pg. 573

Fain, J., Erramli, H., Miallier, D., Montret, M., Sanzelle, S., 1991. Datation par thermoluminescence d'un appareil volcanique trachytique : le Puy de Dôme. Cahiers du Quaternaire 16, 53–62.

Fain, J., Miallier, D., Montret, M., Sanzelle, S., 1988. Zircon Dating: regeneration and evaluation of the external dose. Nucl. Tracks Radiat. Meas. 14/1-2, 333–337.

Fisher, R.A., 1953. Dispersion on a sphere. Proceedings of the Royal Society of London, Series A, 217, pg 295-305

France, L., Demacon, M., Gurenko, A.A., Briot, D., Lithos (2016), Oxygen isotopes reveal crustal contamination and a large, still partially molten magma chamber in Chaine des Puys (French Massif Central) Lithos. Vol. 260, pp. 328-338 DOI: 10.1016/j.lithos.2016.05.013

Gorshkov GS (1959) Gigantic eruption of the volcano Bezymianny, Bull Volcanol 20: 77-109

Gradstein, F.M., Ogg, J.G., Schmitz, M.D., and Ogg, G.M., editors, 2012, The Geologic Time Scale 2012, vol. 1: Boston, Elsevier, 1144 p., http://dx.doi.org/10.1016 /B978-0-444-59425-9.01001-5.

Hagstrum, J.T., Hoblitt, R.P., Gardner, C.A. Gray, T.E., 2002. Holocene geomagnetic secular variation recorded by volcanic deposits at Mount St. Helens, Washington. Bulliten of Volcanology, 63, 8, 545-556.

Hopkinson, J., 1889, Magnetic and Other Physical Properties of Iron at a High Temperature. Philosophical Transactions of the Royal Society of London. A 180 : 443–465.

Hrouda, F., 2002. Low-field variation of magnetic susceptibility and its effect on the anisotropy of magnetic susceptibility of rocks. Geophys. J. Int., 150, 715-723.

Jackson, M., Moskowitz, B., Rosenbaum, J., and Kissel, C., 1998, Field dependence of AC susceptibility in titanomagnetite, Earth Planet. Sci. Lett., 157, 129– 139.

Jelinek, V., 1981. Characterization of the magnetic fabric of rock. Tectonophysics, Volume 79, pp. 63-67.

Jerram, D., Scarth, A., Tanguy, J-C., 2017. Volcanoes of Europe, Dunedin, Edinburgh 278 pp.

Juvigné, e., and Gewelt, M., 1987 la Narse d'Ampoix comme téphrostratotype dans la Chaîne des Puys méridonale (France). Bulletin De L'assosication Francaise Des Etudes Quatenaire 1,37-49.

Katsui Y, Komuro H, Uda T., 1985. Development of faults and growth of Usu-Shinzan cryptodome in 1977-1982 at Usu Volcano, North Japan. Journal of the Faculty of Science, Hokkaido University. Series 4, Geol Mineral, 21(3): 339-362

Kereszturi G, Németh K, 2012, Monogenetic Basaltic Volcanoes: Genetic Classification, Growth, Geomorphology and Degradation, Updates in Volcanology DOI: 10.5772/51387 .

Kirschvink, J.L., 1980. The least-square line and plane and the anaylsis of paleomagnetic data – examples from Siberia and Morocco. Geophysical Journal of the Royal Astronomical Society, 62, pp.669-718

Le Corvec, N.K., Bernhard Spörli, B., Rowland, J., et Jan Lindsay, J., 2013 Spatial distribution and alignments of volcanic centers: Clues to the formation of monogenetic volcanic fields ». Earth-Science Reviews 124, no 0 (2013): 96-114. doi:10.1016/j.earscirev.2013.05.005

Magee, C., Bastow, Jackson, C.A-L, van Wyk de Vries, B., Hetherington, R., Hagos, M., Hogett, M., (2017) Structure and dynamics of surface uplift induced by incremental sill emplacement. Geology 45 (5): 431-434.

Mailler, D., Boivin, P., Deniel, C., Gourgaud, A., Lanos, P., Sforna, M., Pilleyre, T., 2010. The ultimate summit eruption of Puy de Dôme volcano (Chaîne des Puys, French Massif Central) about 10,700 years ago. Comptes Rendus Geoscience, Volume 342, pp.847-854.

Maillier D, Pilleyre T, Boivin P, Sanzele, S., 2013, L'éruption phréatomagmatique du Montchié, Chaîne des Puys, MCF. Quatenaire 24:99-107.

Maillier D, Pilleyre T, Sanzele S, Boivin P, Lanos P., 2012 Revised chronology of the youngest volcanoes of the Chaîne des Puys, French Massif Central. Quatenaire 23:283-290

Martel, C., Champallier, R., Prouteau, G., Pichavant, M., Arbaret, L., Balcone-Boissard, H., Boudon, G., Boivin, P., Bourdier, J-L.; Scaillet, B., (2013) Journal of Petrology, 201306, Vol. 54, Issue 6, pp. 1071-1107 DOI: 10.1093/petrology/egt006

Matheiu, L., van Wyk de Vries, B., 2009, Volcano-tectonic deformation in the Mull Igneous complex. Bulletin of Volcanology 71: 1133-1148 .

McFadden, P.L., and Lowes, F.J., 1981, The discrimination of mean directions drawn from fisher distributions: Geophysical Journal of the Royal Astronomical Society, 67, p. 19-33.

Merrill, RT and McElhinny, MW., 1983, The Earth's Magnetic Field, London, Academic Press.

Michon, L., Merle, O., 2001, The evolution of the Massif Central Rift; spatio-temporal distribution of the volcanism. Bull Soc géol France 172: 201–211.

Minakami, T., Ishikawa, T., and Yagi, K., 1951, The 1944 eruption of Volcano Usu in Hokkaido, Japan. Bull Volcanol 11:45-160.

Moore JG, Albee WC (1981) Topographic and structural changes, March-July 1980 Photogrammetric data. US Geol Surv Prof Pap 1250:123-134

Moskowitz, B.M., R.B. Frankel, and D.A. Bazylinski, 1993, Rock magnetic criteria for the detection of biogenic magnetite, Earth Planet. Sci. Lett., 120, 283-300, 1993.

Nakada, S., 2018, What should we do in Global Geoparks to reduce risks from geohazards. 8th International UNESCO Global Geopark Conference, in Geohazards Workshop. Madonna di Campiglio, Italy 4-8 sept. Abstract Book p62 https://www.campigliodolomiti.it/en/pagine/dettaglio/ggn_content,188/the_abstracts_book,1336.html.

Németh, K., 2010, Monogenetic volcanic fi elds: Origin, sedimentary record, and relationship with polygenetic volcanism, in Cañón-Tapia, E., and Szakács, A., eds., What Is a Volcano?: Geological Society of America Special Paper 470, p. 43–66, doi: 10.1130/2010.2470(04).

Okada, J., H., Mimatsu, S., Fontiela, J., Okada H., 2016, Long run communication support based on diagnostic symptom to the eruption as key roles of volcanologists toward sleeping giant - Case studies from Bandai, Usu and Azores. Abstract. Cities on Volcanoes 9. (*www.citiesonvolcanoes9.com/en)*

Özdemir, Ö., and D.J. Dunlop, 2003. Low-temperature behaviour and memory of iron-rich titanomagnetites (Mt. Haruna, Japan and Mt. Pinatubo, Philippines). Earth Planet. Sci. Lett., 216, 193-200.

Özdemir, Ö., B.M. Moskowitz, and D.J. Dunlop, 1993. The effect of oxidation on the Verwey transition in magnetite. Geophys. Res. Lett., 20, 1671-1674.

Pagli, C., Wright, T.J., Ebinger, C.J., Yun, S.-H., Cann,J.R., Barnie, T., and Ayele, A., 2012, Shallow axial magma chamber at the slow-spreading Erta Ale Ridge: Nature Geoscience, v. 5, p. 284–288, doi: 10 .1038 /ngeo1414.

Petronis, M.S., Delcamp, A., van Wyk de Vries, B., 2013, Magma emplacement into the Lemptégy scoria cone (Chaîne Des Puys, France) explored with structural, anisotropy of magnetic susceptibility, and Paleomagnetic data. Bull Volcanol 75:753

Portal, A., Gailler, L., Labazuy, P., Lénat, J.F. 2016, Geophysical imaging of the inner structure of a lava dome and its environment through gravimetry and magnetism. Journal of Volcanology and Geothermal Research vol. 320: 88-99, DOI:10.1016/j.jvolgeores.2016.04.012

Reeves, J., Macgee, C., Jackson, C-L., (2018) Unravelling intrusion-induced forced fold kinematics and ground deformation using 3D seismic reflection data. Volcanica 1(1): 1 – 17. doi: 10.30909/vol.01.01.0117

Shea, T., van Wyk de Vries, B., 2007, The emplacement of two contrasting debris avalanches at Mombacho Volcano, Nicaragua Bulletin of volcanology 70: 899-921

Smirnov, A. V., 2009, Grain size dependence of low-temperature remanent magnetization in natural and synthetic magnetite: Experimental study, Earth Planets Space, 61, 119-124

Tarling, D. and Hrouda, F., 1993. The Magnetic Anisotropy of Rocks. London: Chapman & Hall Publishing.

Tauxe, L., 1998. Paleomagnetic principles and practices. Kluwer Academic Publishers, Dodrecht, Boston, London.

Tobita, M., Murakami, M., Nakagawa, H., Yarai, H., Fujiwara, S., Rosen, P.A., (2001) 3-D surface deformation of the 2000 Usu Eruption measured by matching of SAR images. Geophys Res Letts, 28(22):4291-4294

Valentine, G.A., Cortés, J.A., Wisdom, E., Smith, E.I., Rasoazanamparany, C., Johnsen, R., Briner, J.P., Harp A.G., Turrin, B., 2018, Lunar Crater volcanic field GEOSPHERE Research Paper

van Wyk de Vries, B., Marques, A., Herrera, R., Granjas, J.L., Llanes, P., Delcamp,A., 2014, Craters of Elevation Revisited : Forced Folds, Bulges and Uplift of Volcanoes (2014) Bulletin of Volcanology DOI: 10.1007/s00445-014-0875-x

van Wyk de Vries, B., Tiu, G., Mossoux, S., Kervyn, M., Lagmay, A.M.A., 2012. Structural control of the Limagne Fault on the Chaîne des Puys. San Francisco, American Geophysical Union, Fall Meeting 2012.

Verwey, E. J., 1939, Electronic conduction of magnetite (Fe3 O4) and its transition point at low temperature, Nature, 144, 327-328.

von Buch, L., (1820) Uber die Zusammenensetzung der basaltischen Inseln und über Ehrebungs-Cratere, Prussian Academy of Sceince.

Závada, P., Kratinová, Z., Kushbach, V. & Shulmann, K., 2009. Internal fabric development in complex lava domes. Tectonopysics, Volume 466, pp. 101-113.

Zijderveld, J.D.A., 1967, A.C. Demagnetization of rocks: Analysis of results, *in:* Methods in Paleomagnetism, D.W. Collinson, K.M. Creer, and S.K. Runcorn, ed., pp. 254, 286, Elsevier, Amsterdam.

APPENDIX FIGURES AND TABLES

Appendix Table 1: Anisotropy of Magnetic Susceptibility Data from the Puy de Dôme. Explanation: N_o = number of accepted specimens; N = number of specimens analyzed at each site; K_m = mean bulk susceptibility; K_1, K_2, and K_3 = trend and plunge (in degrees) of maximum, intermediate, and minimum susceptibility axes; K_1-K_2 = strike and dip of the magnetic foliation plane; L = ratio of K_1/K_2; F = ratio of K_2/K_3; P_j = corrected anisotropy degree; T = shape parameter; ellipsoid shape, O = oblate, P = prolate; UTM coordinates datum WGS 84

Appendix Figure 1. Anisotropy of Magnetic Susceptibility Results

Anisotropy of Magnetic Susceptibility data from each site in the Puy de Dôme. Each diagram is a lower hemisphere equal area projection of the K1, K2, K3 susceptibility axis.

Appendix Table 2. Curie Point Estimates

EXPLANATION: Site, site name; Low Temperature, the first Curie point reached, Inflection Point, Curie Point defined after Tauxe (1998); Hopkinson Peak, Curie point defined after Hopkinson (1889); Ti-Content, estimated Ti content with the titanomagnetite phase after Akimoto (1962).

Appendix Figure 2: Curie Point Estimate Heating-Cooling Diagrams

EXPLANATION: Red = Heating Curve; Blue = Cooling Curve; T[°C] = temperature in degrees Celsius; Kt [E-6] = bulk susceptibility x 10^{-6} SI

Appendix Figure 3. Isothermal Remanent Magnetization Results

(A) All IRM acquisition curves are steep and reach ~ 85% saturation by ~0.40 T with the remaining 15% of the magnetization acquired up to 2.5 T. The results indicate a dominance of magnetite, likely single domain titanomagnetite of a restricted grain size, along with the presence of titanomaghemite and hematite (Özdemir and Dunlop, 1993).

Appendix Figure 4. Low Temperature Remanence Experiments

(B) All MPMS results yield similar curves on warming yet the absolute intensity of the magnetization remanence varies between the three representative samples. All show a suppressed Verwey transition (Verwey, 1939) indicative of non stoichiometric behavior. Ti cation substitution or partial oxidation can lower the transition temperature or suppress it entirely (Özdemir et al., 1993). We see no evidence of a hematite Morin transition.

Appendix

1. Anisotropy of Magnetic Susceptibility Methods and Results and Rock Magnetic data

Analytical Methods

Anisotropy of Magnetic Susceptibility Methods

Anisotropy of magnetic susceptibility (AMS) measurements of a rock specimen yield an ellipsoid of magnetic susceptibility (K) defined by the length and orientation of its three principal axes, $K_1 \geq K_2 \geq K_3$, which are the three eigenvectors of the susceptibility tensor (Tarling and Hrouda 1993). The long axis of the magnetic susceptibility ellipsoid, K_1, gives the magnetic lineation, while the short axis, K_3, defines the normal to the magnetic foliation plane (K_1-K_2). The bulk magnetic susceptibility (K_m) is the arithmetic mean of the principal axes K_1, K_2, and K_3 (see Jelínek 1981; Tarling and Hrouda 1993). We measured the AMS of 332 specimens prepared from samples collected at 17 sites distributed throughout the study area. The AMS measurements were performed on an AGICO MFK1-A multi-function kappabridge operating at low alternating field of 200 A/m at 976 Hz at the New Mexico Highlands University Paleomagnetic-Rock Magnetic laboratory. The AMS results and the susceptibility parameters are summarized in **Table Appendix 1**.

Appendix Table 1: Anisotropy of Magnetic Susceptibility Data from the Puy de Dome

Site	No	N	Km (10-3 SI)	K1	K2	K3	K1-K2	L	F	Pj	T	Shape	UTM WGS 84 Easting	Northing
PDD1	24	24	9.81	184/08	092/15	302/76	032/14E	1.005	1.006	1.011	0.048	O	496894.9	5068463.8
PDD2	20	22	3.46	037/71	281/09	188/17	278/73N	1.006	1.106	1.127	0.882	O	496918.9	5067416.8
PDD3	13	13	1.59	243/73	060/17	101/01	191/89W	1.066	1.088	1.159	0.778	O	496959.5	5068514.9
PDD4	17	17	4.43	192/47	311/24	058/33	148/57W	1.005	1.055	1.067	0.816	O	496930.4	5068407.1
PDD5	24	25	4.47	005/31	193/59	097/04	187/86W	1.003	1.022	1.028	0.750	O	496841.9	5068443.7
PDD6	14	16	3.77	288/08	044/72	195/16	285/74N	1.020	1.043	1.065	0.357	O	496978.1	5068907.1
PDD7	17	17	3.30	202/14	297/18	076/67	166/23W	1.008	1.041	1.054	0.658	O	496854.2	5068508.9
PDD8	12	12	2.74	216/47	352/35	100/23	190/67W	1.011	1.002	1.014	-0.654	P	496853.4	5068555.9
PDD9	22	22	2.55	172/61	063/10	328/27	058/63S	1.009	1.135	1.164	0.870	O	497053.8	5068497.5
PDD10	20	20	3.59	075/49	342/03	250/41	340/49E	1.010	1.026	1.038	0.467	O	496799.9	5068479.2
PDD11	14	14	4.35	019/20	125/38	297/46	027/44E	1.004	1.023	1.029	0.677	O	497068.6	5068482.2
PDD12	15	19	0.52	351/58	221/02	130/32	220/58W	1.012	1.019	1.032	0.232	O	497175.6	5068478.4
PDD13	17	17	0.40	333/26	227/28	098/50	188/40W	1.012	1.014	1.027	0.089	O	496879.2	5068477.2
PDD14	16	16	6.97	070/45	193/29	303/31	033/59E	1.022	1.088	1.119	0.596	O	496930.9	5068920.6
PDD15	22	24	0.96	305/52	127/38	036/01	126/89S	1.007	1.008	1.015	0.052	O	497617.9	5068642.0
PDD16	21	21	0.24	274/58	094/33	004/00	094/90S	1.016	1.031	1.048	0.309	O	496968.1	5068920.0
PDD17	31	33	0.48	199/45	302/42	032/49	122/41S	1.016	1.105	1.134	0.725	O	497053.2	5068940.7

Appendix Table 1: Anisotropy of Magnetic Susceptibility Data from the Puy de Dôme. Explanation: N_o = number of accepted specimens; N = number of specimens analyzed at each site; K_m = mean bulk susceptibility; K_1, K_2, and K_3 = trend and plunge (in degrees) of maximum, intermediate, and minimum susceptibility axes; K_1-K_2 = strike and dip of the magnetic foliation plane; L = ratio of K_1/K_2; F = ratio of K_2/K_3; P_j = corrected anisotropy degree; T = shape parameter; ellipsoid shape, O = oblate, P = prolate; UTM coordinates datum WGS 84

Anisotropy of Magnetic Susceptibility Results

Appendix Figure 1. Anisotropy of Magnetic Susceptibility Results

EXPLANATION: Anisotropy of Magnetic Susceptibility data from each site in the Puy de Dome. Each diagram is a lower hemisphere equal area projection of the K1, K2, K3 susceptibility axis.

PDD1

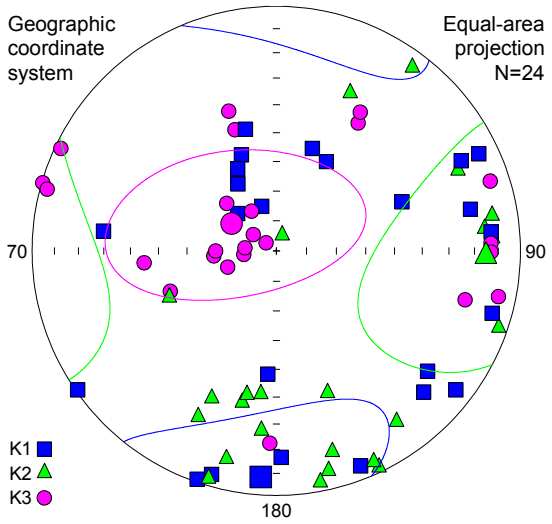

PDD2

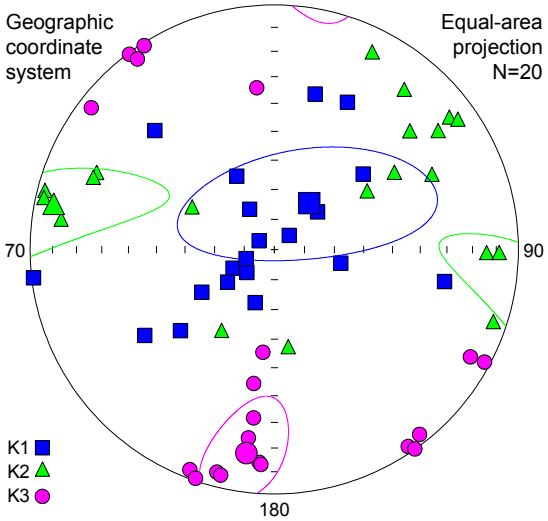
Geographic
coordinate
system
Equal-area
projection
N=20
70
90
180
K1
K2
K3

PDD3

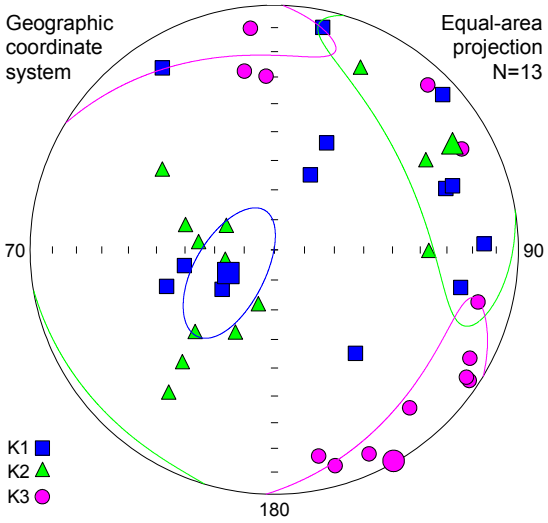
Geographic
coordinate
system
Equal-area
projection
N=13
70
90
180
K1
K2
K3

PDD4

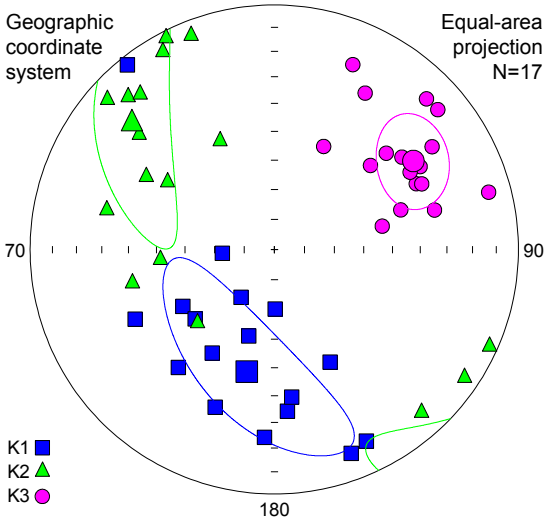
Geographic
coordinate
system
Equal-area
projection
N=17
70
90
180
K1
K2
K3

PDD5

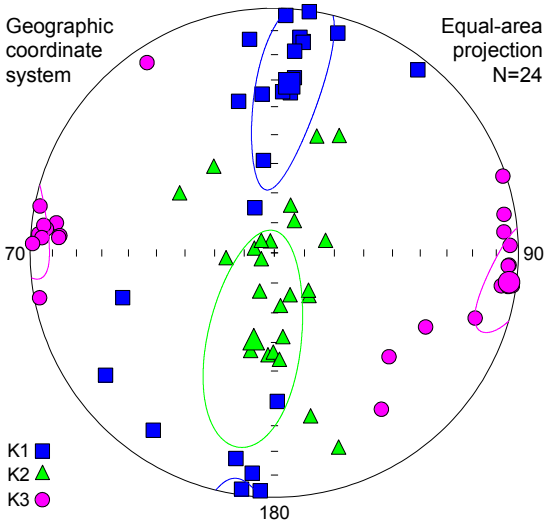
Geographic
coordinate
system
Equal-area
projection
N=24
70
90
180
K1
K2
K3

PDD6

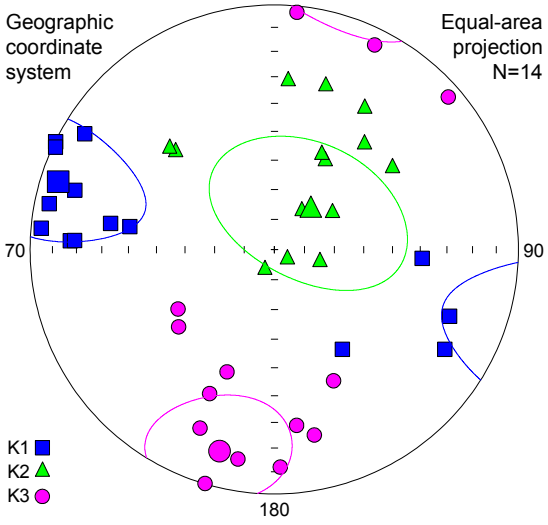
Geographic
coordinate
system
Equal-area
projection
N=14
70
90
180
K1
K2
K3

PDD7

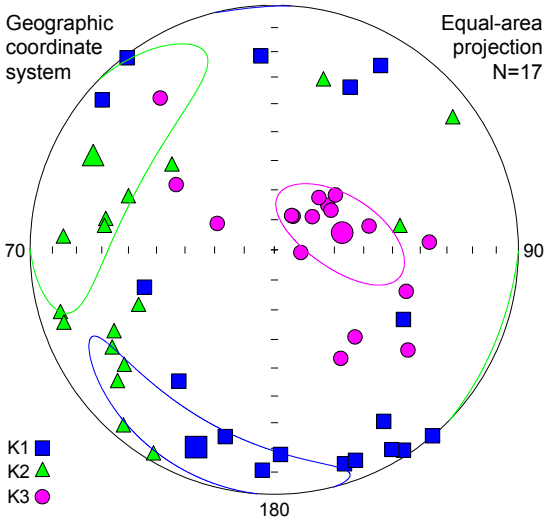
Geographic
coordinate
system
Equal-area
projection
N=17
70
90
180
K1
K2
K3

PDD8

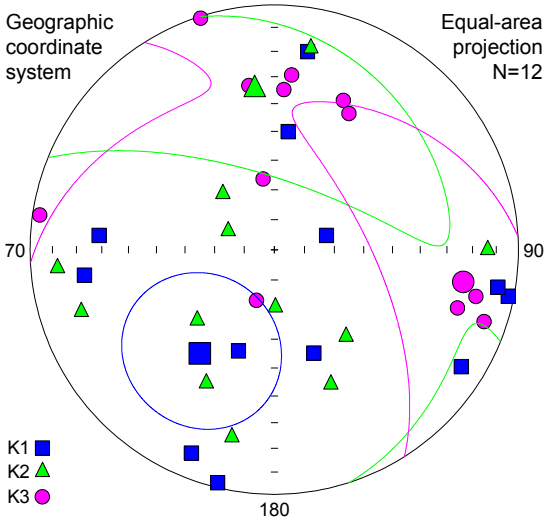
Geographic
coordinate
system
Equal-area
projection
N=12
70
90
180
K1
K2
K3

PDD9

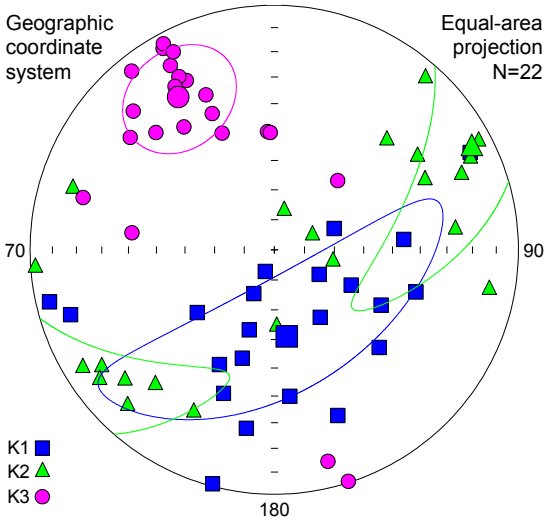
Geographic
coordinate
system
Equal-area
projection
N=22
70
90
180
K1
K2
K3

PDD10

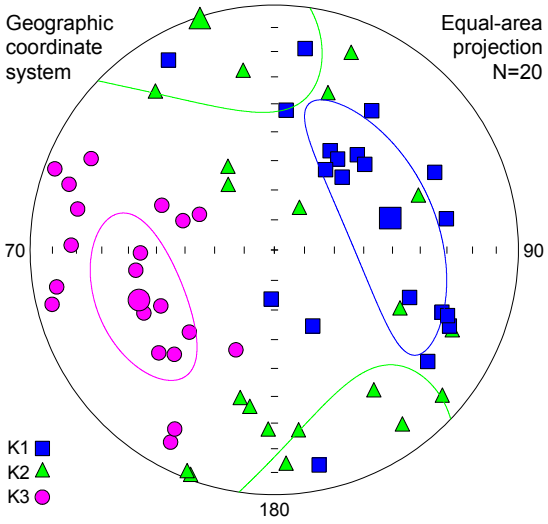
Geographic
coordinate
system
Equal-area
projection
N=20
70
90
180
K1
K2
K3

PDD11

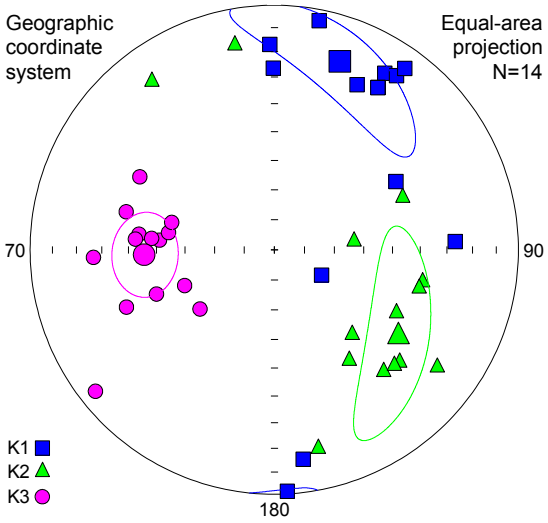
Geographic
coordinate
system
Equal-area
projection
N=14
70
90
180
K1
K2
K3

PDD12

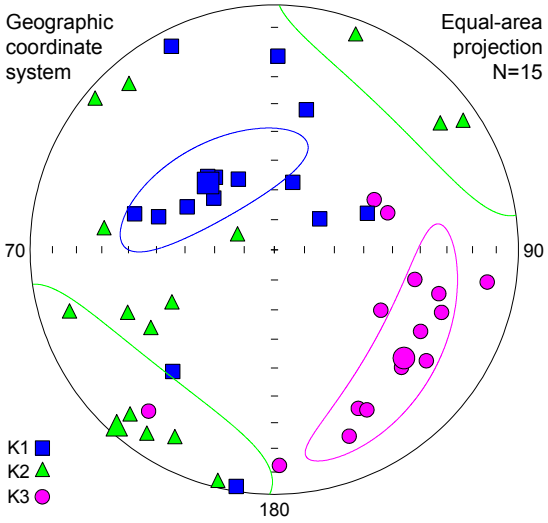
Geographic
coordinate
system
Equal-area
projection
N=15
70
90
180
K1
K2
K3

PDD13

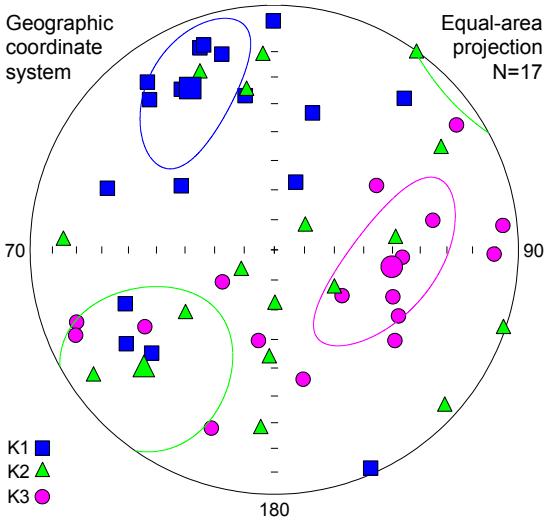
Geographic
coordinate
system
Equal-area
projection
N=17
70
90
180
K1
K2
K3

PDD14

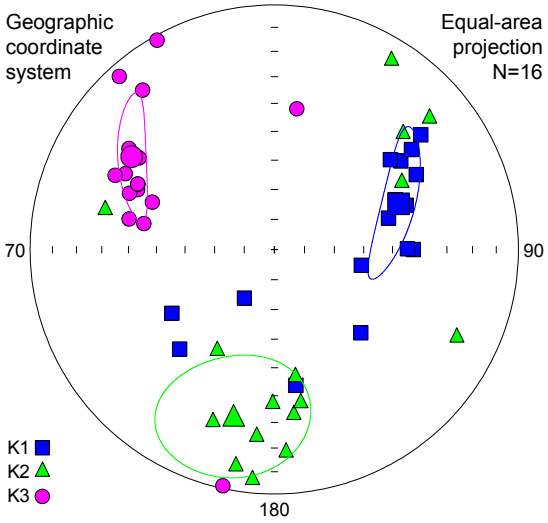
Geographic
coordinate
system
Equal-area
projection
N=16
70
90
180
K1
K2
K3

PDD15

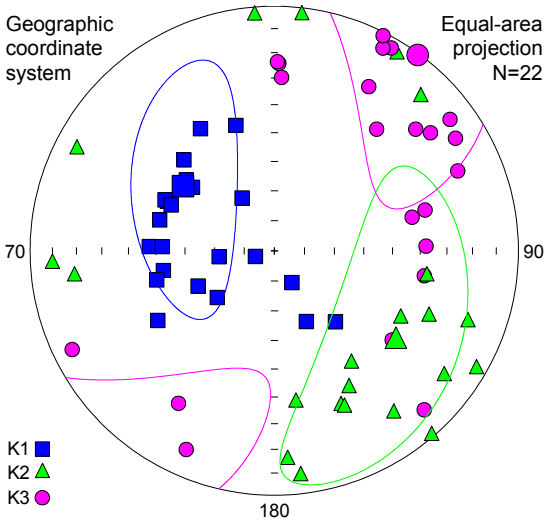
Geographic
coordinate
system
Equal-area
projection
N=22
70
90
180
K1
K2
K3

PDD16

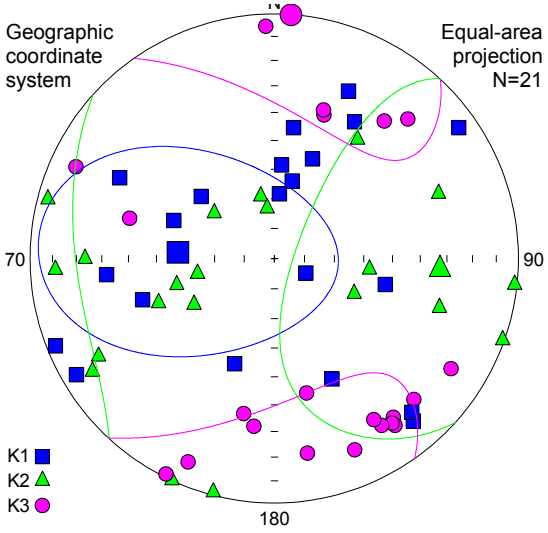
Geographic
coordinate
system
Equal-area
projection
N=21
70
90
180
K1
K2
K3

PDD17

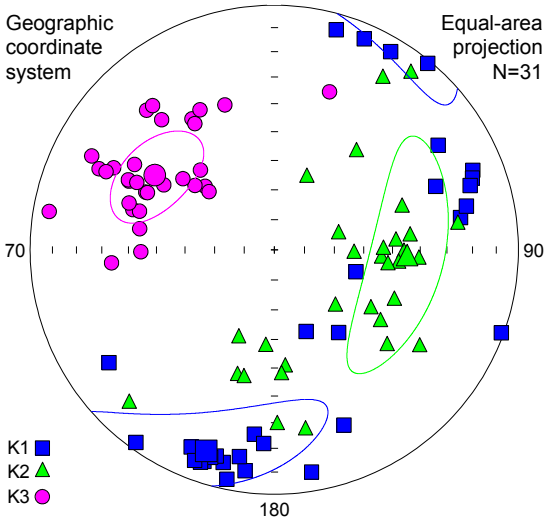
Geographic
coordinate
system
Equal-area
projection
N=31
70
90
180
K1
K2
K3

5

Rock Magnetic Results

Curie Point Estimates

Appendix Table 2: Curie Point Estimates

Site	Low Temperature	Inflection Point	Hopkinson Peak	Ti - Content
PDD - 1C	-	558	499*	0.1360
PDD - 2B	-	576*	-	0.0110
PDD - 3F	-	582*	-	0.0005
PDD - 4B	-	582*	386	0.0005
PDD - 5K	289	584*	-	0.0028
PPD - 6H	-	494*	-	0.1440
PPD - 7L	-	491*	-	0.1480
PPD - 8A	-	-	488*	0.1450
PPD - 9E	-	588*	-	0.0094
PPD - 10J	-	574*	-	0.0140
PPD - 12G	267	-	477*	0.1710
PPD - 13J	425	587	513*	0.1140

*preferred Curie point estimate in degrees Celsius

Appendix Figure 2: Curie Point Estimate Heating-Cooling Diagrams

EXPLANATION: Red = Heating Curve; Blue = Cooling Curve; T[°C] = temperature in degrees Celsius; Kt [E-6] = bulk susceptibility x 10-6 SI

PDD - 1C

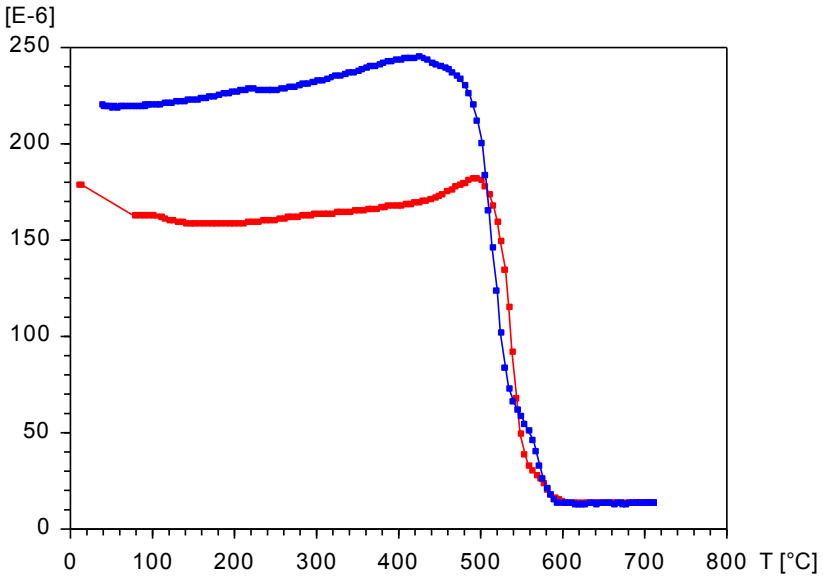

PDD - 2B

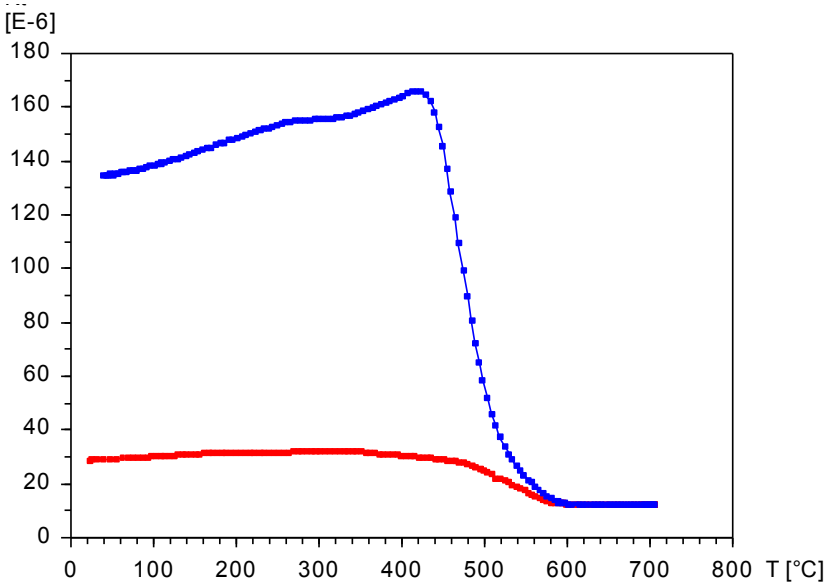

PDD - 3F

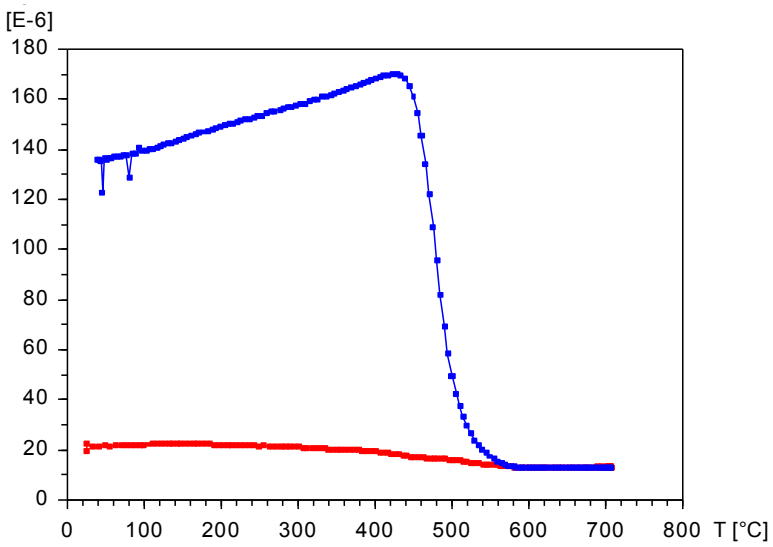
[E-6]
180
160
140
120
100
80
60
40
20
0
0
100
200
300
400
500
600
700
800
T [°C]

PDD - 4B

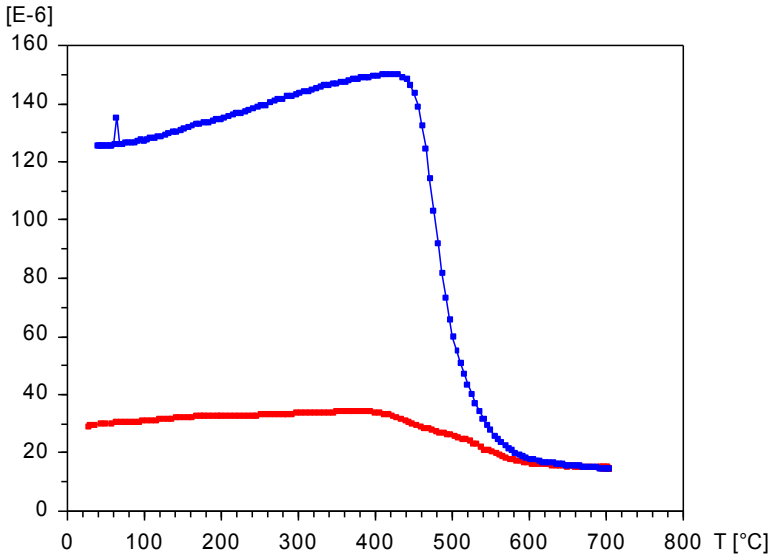
[E-6]
160
140
120
100
80
60
40
20
0
0
100
200
300
400
500
600
700
800
T [°C]

PDD - 5K

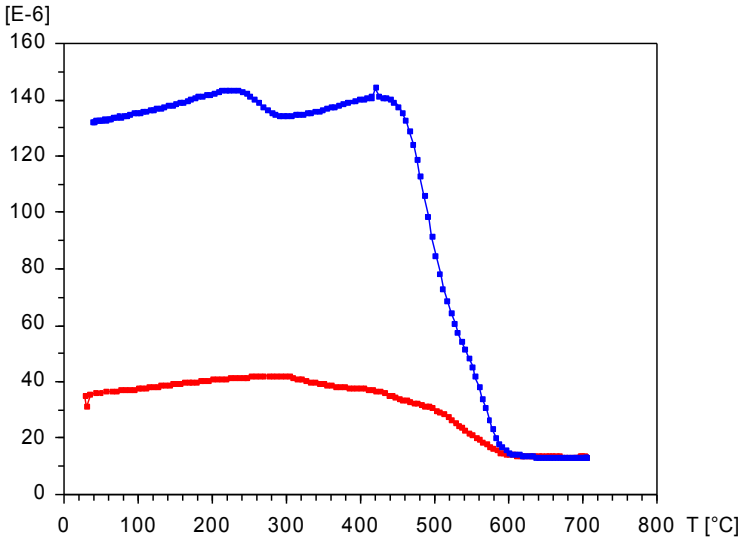
[E-6]
160
140
120
100
80
60
40
20
0
0
100
200
300
400
500
600
700
800
T [°C]

PDD - 6H

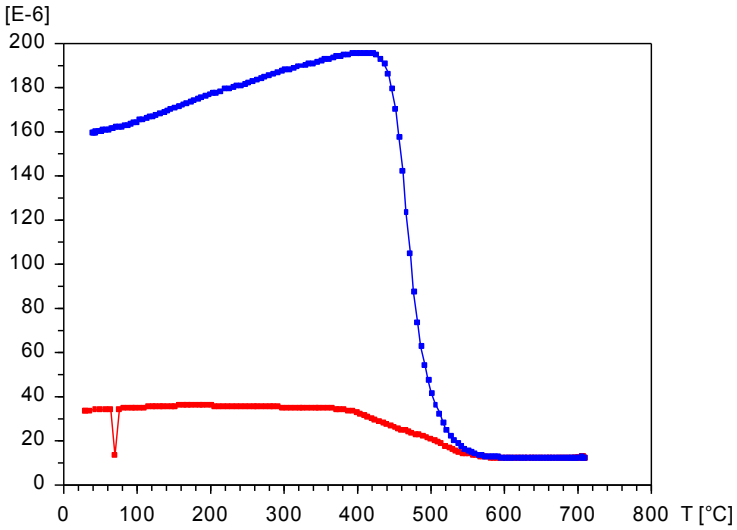
[E-6]
200
180
160
140
120
100
80
60
40
20
0
0
100
200
300
400
500
600
700
800
T [°C]

PDD - 7L

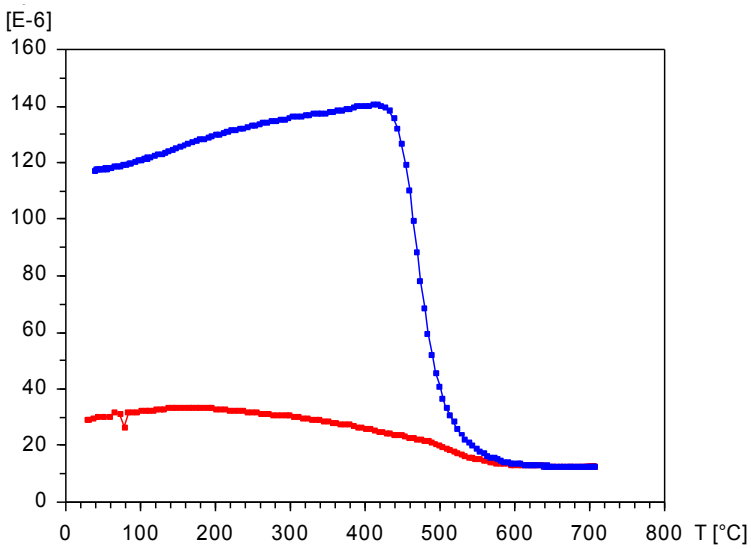
[E-6]
160
140
120
100
80
60
40
20
0
0
100
200
300
400
500
600
700
800
T [°C]

PDD - 8A

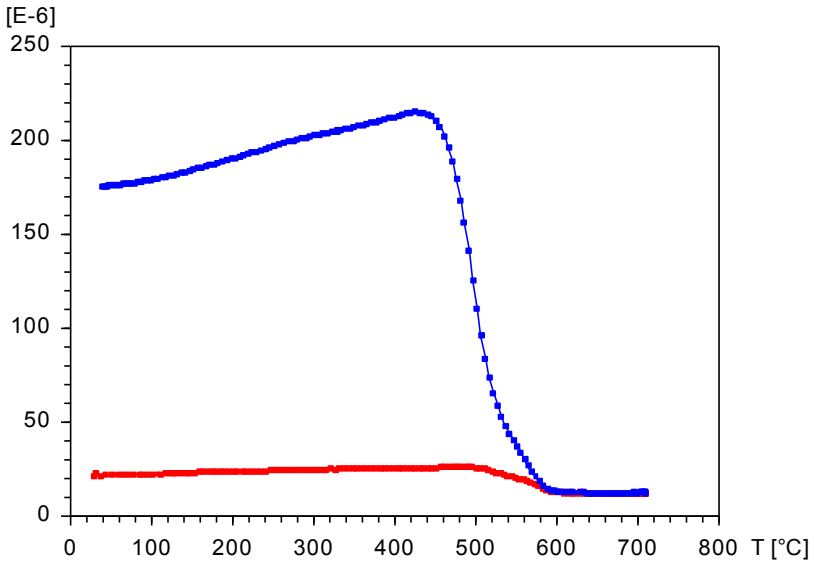
[E-6]
250
200
150
100
50
0
0
100
200
300
400
500
600
700
800
T [°C]

PDD - 9E

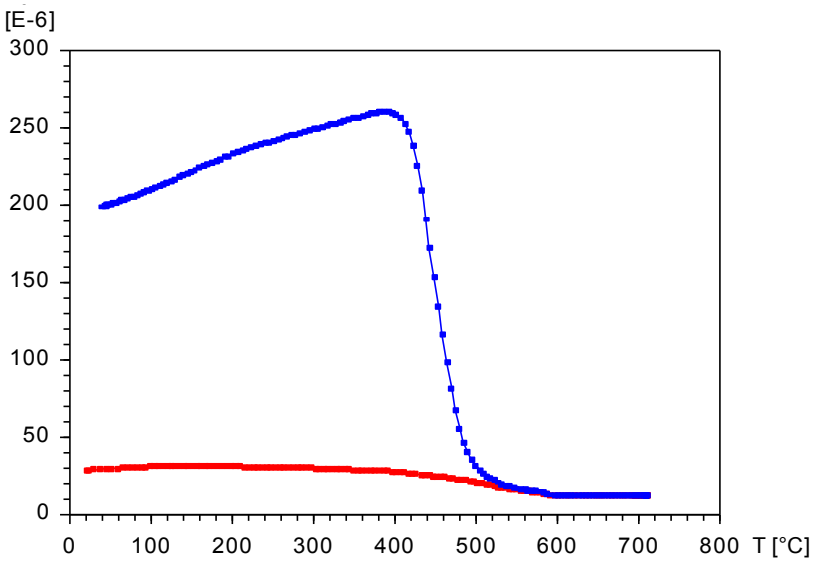

PDD - 10J

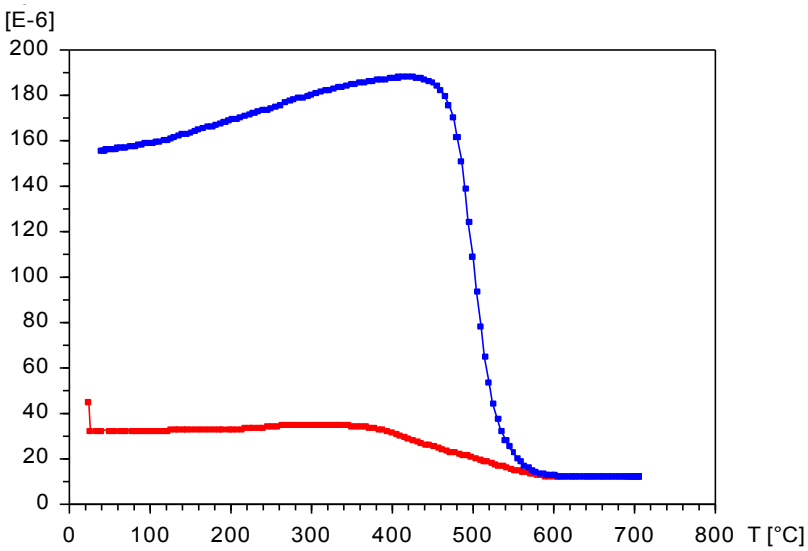

PDD - 11P

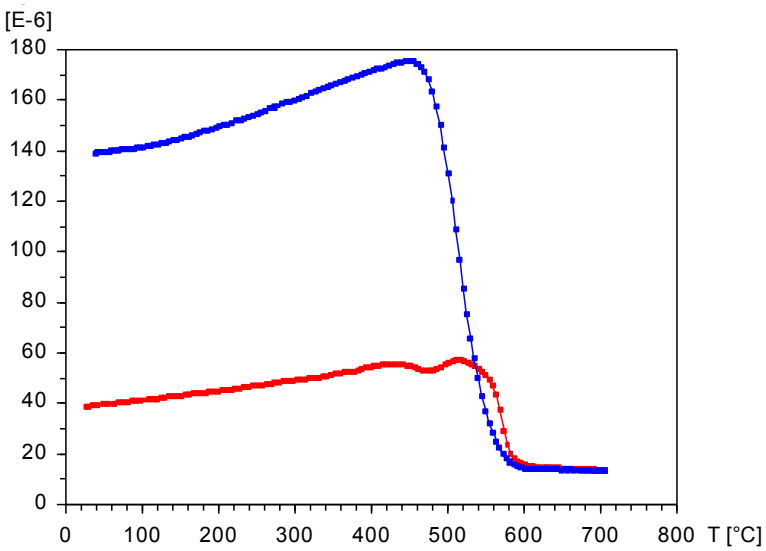

PDD - 12G

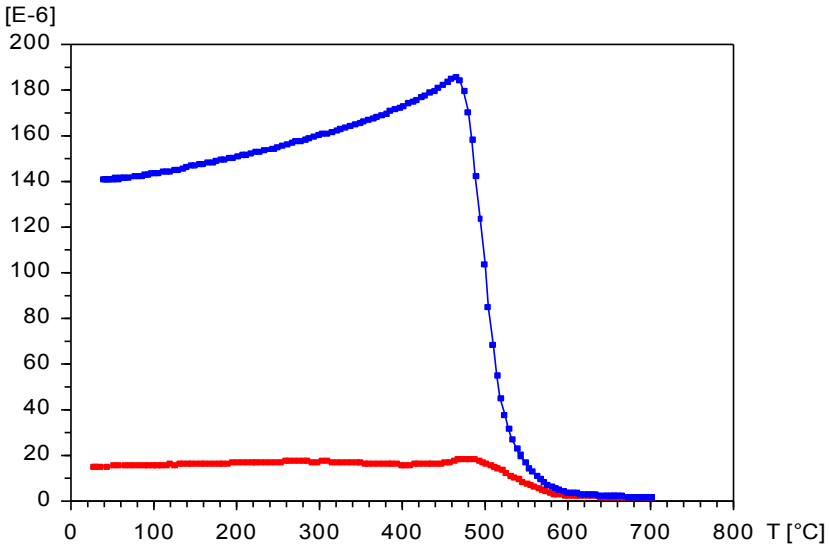

PDD - 13J

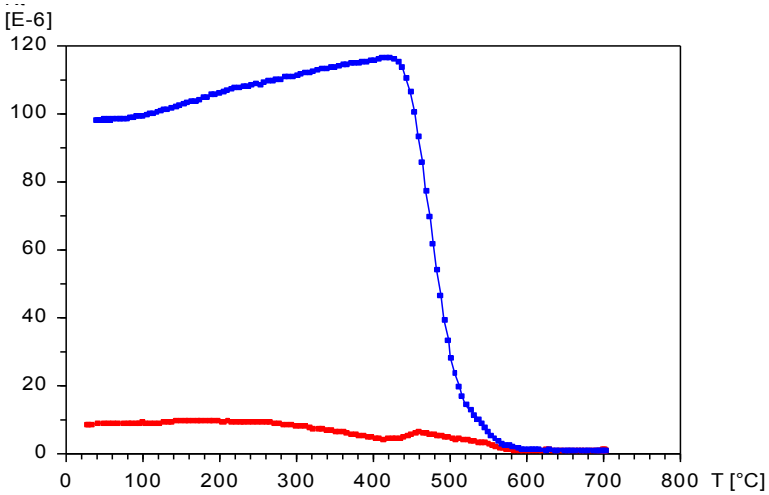
[E-6]
120
100
80
60
40
20
0
0
100
200
300
400
500
600
700
800
T [°C]

Isothermal Remanent Magnetization Results

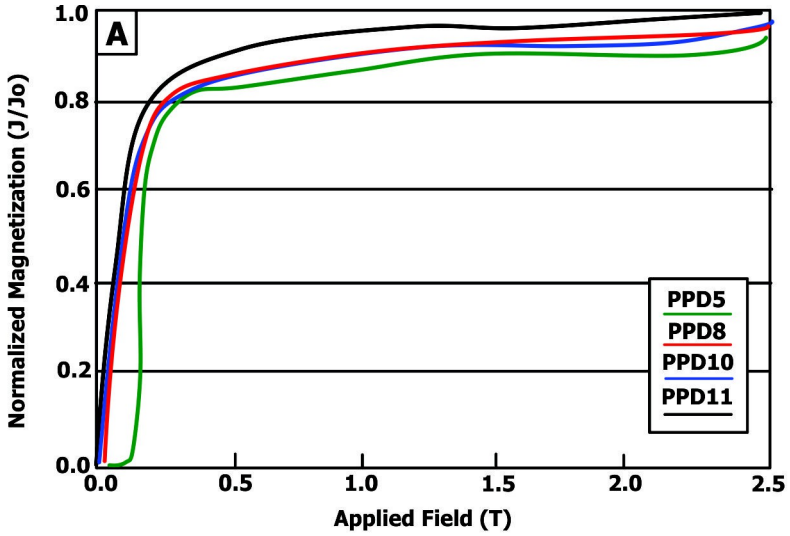

Appendix Figure 3. Isothermal Remanent Magnetization Results

(A) All IRM acquisition curves are steep and reach ~ 85% saturation by ~0.40 T with the remaining 15% of the magnetization acquired up to 2.5 T. The results indicate a dominance of magnetite, likely single domain titanomagnetite of a restricted grain size, along with the presence of titanomaghemite and hematite (Özdemir and Dunlop, 1993).

Low Temperature Remanence Experiments

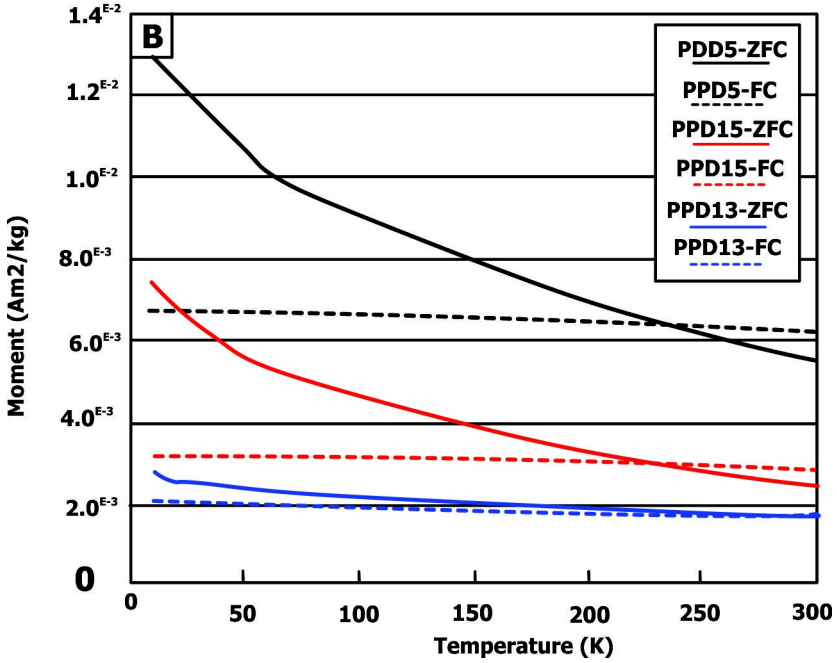

Appendix Figure 4. Low Temperature Remanence Experiments

(B) All MPMS results yield similar curves on warming yet the absolute intensity of the magnetization remanence varies between the three representative samples. All show a suppressed Verwey transition (Verwey, 1939) indicative of non stoichiometric behavior. Ti cation substitution or partial oxidation can lower the transition temperature or suppress it entirely (Özdemir et al., 1993). We see no evidence of a hematite Morin transition.